Summer 2024

Solution Combustion Synthesis and Characterization of Fumarolic Mineral Dolerophanite, Copper (II) Oxide Sulfate

Eric J. Cyganowski
University of Texas at Arlington

SOLUTION COMBUSTION SYNTHESIS AND CHARACTERIZATION OF FUMAROLIC MINERAL DOLEROPHANITE, COPPER (II) OXIDE SULFATE

by

ERIC JOSEPH CYGANOWSKI

THESIS

Submitted in partial fulfillment of the requirements for the
degree of Master of Science in Chemistry at
The University of Texas at Arlington
August 2024

Arlington, Texas

Supervising Committee:

Krishnan Rajeshwar, Supervising Professor
Rasika Dias
Frederick M. MacDonnell

DEDICATION

This work is dedicated to my family and friends who supported me throughout this journey and helped provide the encouragement and motivation needed to persevere. Without you, this would not have been possible – thank you.

ACKNOWLEDGEMENTS

At the outset of this thesis, I would like to acknowledge my appreciation to those whose unwavering encouragement and support have been integral to its completion. These individuals are the ones who have had the most profound impact on my journey as both a student and researcher in my graduate career.

I would first like to express my deepest gratitude by acknowledging my supervising professor, Dr. Krishnan Rajeshwar for his invaluable guidance, expertise, and support throughout my academic career. I first met Dr. Rajeshwar when I was an undergraduate and it was his passion for electrochemistry and solid-state chemistry that drew me to pursue those fields. When it came time to choosing a supervising professor, I had no doubt in my mind that he would be the best fit. His insightful feedback and encouragement these last few years significantly contributed to the development and completion of this work. His mentorship has been instrumental in the shaping of my academic and professional growth and as such I am honored to have been a researcher in his group.

I would also like to express my gratitude for the members of my thesis defense committee, Dr. Rasika Dias and Dr. Frederick M. MacDonnell, for their invaluable expertise, insightful feedback, and dedicated commitment throughout this entire process. I am indebted to their examination and constructive criticism without which I would not have grown into the researcher I am today. I am also deeply grateful to Dr. Peter Kroll who was originally on my committee but was unable to attend my defense. I, too, first met Dr. Kroll when I was an undergraduate and it was

his teaching that encouraged me to pursue a career in academia. I would like to thank Dr. Kwangho Nam for the selection of my committee.

I would like to give thanks to my peers in the Rajeshwar group. Dr. Fahad I. Danladi and Abhishek Rawat helped provide a strong foundation in my research by providing invaluable training. Abhishek also helped considerably with regards to his connection with collaborators and with regards to help with scanning electron microscopy. Arham Shamim was an excellent classmate for our graduate-level coursework. Katheryn Cruz provided invaluable help with her knowledge and help in performing structure refinement and scanning electron microscopy. And my undergraduate mentee, Vaishnavi Guttikonda, helped carry out and refine the synthesis that was paramount to this work.

I would next like to express how grateful I am to collaborators on this project. The Rajeshwar group collaborates with Dr. Efstathios I. Meletis and his group in the Materials Science and Engineering department; in particular, Chuzhong Zhang from the Meletis group provided help in performing transmission electron microscopy analysis. Dr. Abhishek Kumar Adak from The Abdus Salam International Centre for Theoretical Physics in Trieste, Italy provided the computational theory for this work. I would also like to give a special thanks to Hannah Hayes and Takhya Holley from the Kroll group for not only being willing to help with thermal studies, but also always allowing me to use them as a sounding board for my ideas.

I would like to thank Dr. Roy McDougald and the Shimadzu Institute Center for Nanostructured Materials for providing instrumentation and training invaluable to this work. I would also like to thank Dr. Jiechao Jiang, Dr. Yi Shen, and the Characterization Center for Materials and Biology for further instrumentation and training that was invaluable to this work.

I would like to thank the graduate program coordinator, Mrs. Stephanie Henry, and the graduate academic advisors, Dr. Frank Foss and Dr. Junha Jeon, for their guidance in navigating my graduate career. I would like to thank the undergraduate lab coordinators, Dr. Cynthia Griffith and Mr. Naje Huff, for their support in developing my skills as a teaching assistant. Lastly, I would like to thank Dr. Joe Buonomo and Dr. Jimmy Rogers as the two figures to whom I look up to as role models when it comes to teaching and educating others.

This thesis represents not only the culmination of my Master's student career, but also a testament to the contributions of every individual mentioned here who have generously offered their time, knowledge, and resources. To them, I say thank you.

TABLE OF CONTENTS

LIST OF FIGURES

LIST OF TABLES

LIST OF ABBREVIATIONS

AFMR	Antiferromagnetic Resonance
Atl	Antlerite
ATR	Attenuated Total Reflectance
CB	Conduction Band
Cct	Chalcanthite
CM	Ceramic Method
CNMNC	Commission on New Minerals, Nomenclature and Classifications
CV	Cyclic Voltammetry
CVT	Chemical Vapor Transport
DFT	Density Functional Theory
DOS	Density of States
Dph	Dolerophanite
DRS	Diffuse Reflectance Spectroscopy
DSC	Differential Scanning Calorimetry
EDX	Energy-Dispersive X-Ray Spectroscopy
FTIR	Fourier Transform Infrared Spectroscopy
GGA	Generalized Gradient Approximation
GTFE	Great Tolbachik Fissure Eruption
HS	Hydrothermal Synthesis
HSE	Heyd–Scuseria–Ernzerhof Hybrid Functional

IMA	International Mineralogical Association
Kby	Kobyashevite
PAW	Projector Augmented-Wave
PBE	Perdew–Burke–Ernzerhof Functional
PBEsol	Perdew–Burke–Ernzerhof Functional for Solids
PDOS	Projected Density of Sta
pXRD	Powder X-Ray Diffraction
RE	Reference Electrode
RH	Relative Humidity
SCS	Solution Combustion Synthesis
SEM	Scanning Electron Microscopy
TGA	Thermogravimetric Analysis
UV-vis	Ultraviolet-Visible Spectroscopy
VB	Valence Band
VESTA	Visualization for Electronic and Structural Analysis
XRD	X-Ray Diffraction

ABSTRACT

SOLUTION COMBUSTION SYNTHESIS AND CHARACTERIZATION OF FUMAROLIC MINERAL DOLEROPHANITE, COPPER (II) OXIDE SULFATE

Eric Joseph Cyganowski, M.S.

The University of Texas at Arlington, 2024

Supervising Professor: Krishnan Rajeshwar, Ph.D.

Dolerophanite Cu_2OSO_4 is a rare mineral found almost exclusively in the fumaroles of volcano systems and is sensitive to temperature and humidity conditions. It has a monoclinic *C*2/*m* crystal structure characterized by two-dimensional layers composed of sulfate anions dispersed amongst copper (II) oxide backbones. There has been recent interest in dolerophanite due to the magnetic properties of its Kagome-like lattice as well as its potential use as a photocatalyst or Li-ion battery electrode. Literature on the material however has been limited by the available synthesis strategies. As such, this thesis work presents a novel strategy to produce dolerophanite through a time- and energy-efficient solution combustion synthesis methodology.

Physical analysis provided a comparison of dolerophanite samples prepared by ceramic method and solution combustion synthesis. Thermogravimetric analysis and differential scanning calorimetry were performed to better understand the thermal stability of dolerophanite. Kissinger first-order kinetics model was used to estimate the activation energy for the thermal decomposition

of dolerophanite to copper (II) oxide and to copper (I) oxide. Suggested mechanistic pathways were presented for these decompositions. Kubelka-Munk transformation of the Tauc equation allowed diffuse reflectance data to estimate both direct and indirect optical bandgaps. Density functional theory calculations provided computational evidence for the experimentally observed bandgaps. Fourier transform infrared spectroscopy and Raman spectral data were used to characterize dolerophanite via the nuances in its Cu–O and its S–O bonding framework.

Finally, suggested further experimentation to explore modifications to the solution combustion synthesis as well as potential avenues to explore the applications of dolerophanite were discussed.

CHAPTER 1: INTRODUCTION

1.1 Fumarolic Copper Sulfate Minerals

Fumarolic sulfate minerals refer to those which can be found primarily in the surface vents, or *fumaroles*, of volcano systems and, occasionally, in the remnants of natural underground coal fires.[1] Many of the transition metal sulfates in this class of minerals were identified in 1968 to contain "additional" oxygen atoms (O_a) which do not participate in the "acid residue" sulfate anion complex which have their own oxygen atoms, (O_s).[2] Evidence supports the idea that these additional oxygens, particularly in oxo-centered copper [OCu_4] tetrahedra, are the result of a series of chemical reactions facilitating the transport of chalcophilic copper by fumarolic and volcanic gases, owing to their abundance in this class of minerals.[3] Even in the fumaroles in which they are found, these high-temperature copper sulfate minerals are considered rare and exotic due to their poor stability with respect to temperature conditions, atmospheric relative humidity, and moisture.[4] In spite of this rarity, these compounds are mineralogically fascinating, owed in no small part due to the variety of complex multidimensional crystal structures found in these minerals.[5]

Fumarolic copper sulfates have been known to exist in Mt. Vesuvius in Italy since antiquity; thorough mineralogical studies exist for the identification of the minerals of this region and their formation in this particular oxidative fumarolic environment.[6] In the aftermath of the Great Tolbachik Fissure Eruption (GTFE) in 1975–76, the Tolbachik volcano complex in Russia also became a source of a large number of these copper sulfate minerals; as with those of Vesuvius, the fumarolic minerals of the GFTE have been the subject of thorough mineralogical studies perform.[7]

This class of minerals continues to be extensively explored from both a materials perspective and a magnetic perspective,[8] and as such, this thesis study aims to add to the literature of these compounds by way of an examination of the mineral dolerophanite, Cu_2OSO_4. Mineral symbols used throughout this text are those approved by the International Mineralogical Association (IMA) Commission on New Minerals, Nomenclature and Classifications (CNMNC).[9]

1.2 The Structure of Dolerophanite

Dolerophanite was first identified in 1873 in Italy,[10] and its structure has been known as early as 1940 through both single-crystal X-ray diffraction (XRD) and powder X-ray diffraction (pXRD).[11, 12] Refinement of the structure via electron-density projections was first performed in 1963;[13] further refinement was performed in 1985 and serves as the most cited reference for the dolerophanite structure.[14]

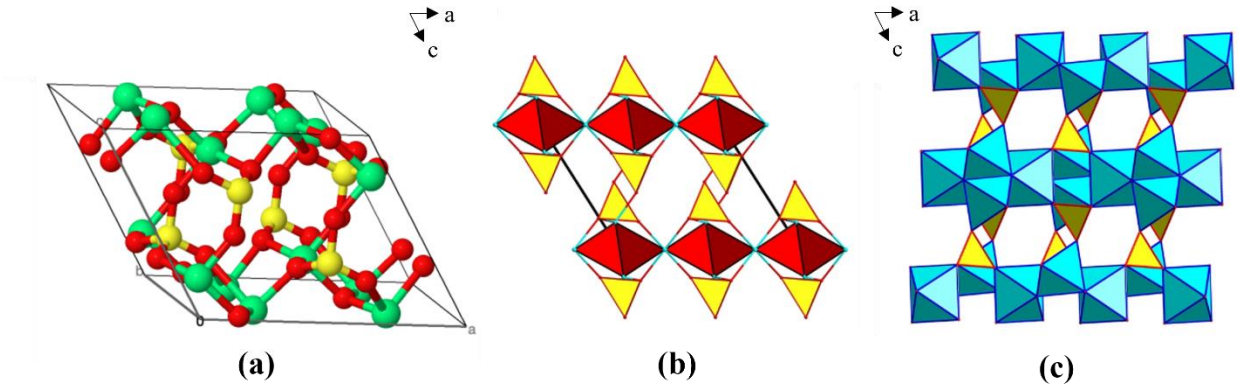

Figure 1-1: (a) Monoclinic unit cell of dolerophanite; (b) dolerophanite as $(SO_4)^{2-}$ tetrahedra (yellow) and $[OCu_2]^{2+}$ tetrahedra (red); (c) dolerophanite as $(SO_4)^{2-}$ tetrahedra (yellow) and a "backbone" of $[CuO_6]$ octahedra and $[CuO_5]$ trigonal bipyramids (both blue); from ref 8.

Dolerophanite has a monoclinic crystal structure with the *C*2/*m* Hermann–Mauguin space group (Figure 1-1a). A summary of the unit cell parameters and their respective reference source can be found in Table 1-1. The compound's structure can be described by two-dimensional (2D)

layers consisting of two basic units: $(SO_4)^{2-}$ tetrahedra dispersed between layers of edge- and corner-sharing oxo-centered $[OCu_2]^{2+}$ tetrahedra dimers (Figure 1-1b).[5] Alternatively, the 2D copper "backbone" can instead be viewed as two symmetrically-independent metal-centered units: a [4 + 2] Jahn-Teller distorted elongated $[CuO_6]$ octahedron centered around the Cu1 atom position and a compressed $[CuO_5]$ trigonal bipyramid centered around the Cu2 atom position (Figure 1-1c).[8] The positions of the Cu1 and Cu2 atom sites within the context of the copper "backbone" can be seen in Figure 1-4. Within the context of "additional" oxygens (O_a), the Cu–O_a bonds present in dolerophanite are shorter and stronger than analogous bonds in $[OCu(II)_4]$ tetrahedra of similar inorganic compounds, owing to the overall strength of the copper "backbone" of the compound.[14] Within the context of the "acid residue" oxygens (O_s), the S–O_s bonds of $(SO_4)^{2-}$ in similar inorganic compounds are known to be stronger than the Si–O bonds in silicates[15] contributing once again to the overall structural stability of dolerophanite.[8]

Table 1-1: Summary of reported cell parameters of dolerophanite [Cu_2OSO_4, *C*2/*m*]. References listed in ascending chronological order.

***a* (Å)**	***b* (Å)**	***c* (Å)**	***α* (°)**	***β* (°)**	***γ* (°)**	***V*(Å^3)**	**Ref.**
9.39	6.30	7.62	90.00	122.415	90.00	—	(11)
9.355	6.312	7.628	90.00	122.175	90.00	—	(12)
9.370	6.319	7.639	90.00	122.34	90.00	382.1	(14)
9.3636	6.3219	7.6305	90.00	122.336	90.00	—	(16)
9.3993	6.3391	7.6688	90.00	122.434	90.00	385.65	(8)

1.3 Reported Synthesis Pathways for Dolerophanite

Naturally occurring dolerophanite samples have been primarily collected from the fumaroles of either Mt. Vesuvius in Italy[11–13] or the Tolbachik volcano complex in Russia.[4, 8] Samples from Vesuvius are semi-quantitatively reported to have cation substitution from both zinc and nickel[13] while those from Tolbachik are quantitatively reported to have cation substitution from zinc, resulting in the presence of a minor zinc oxide phase of up to 1.8 wt %.[4]

The first reported synthesis pathway for dolerophanite was in 1936 via the thermal decomposition of copper (II) sulfate; heating copper (II) sulfate pentahydrate in a muffle furnace at a temperature of ~650 ºC for about 1 h yielded a finely powdered, yellow-brown dolerophanite sample.[12, 17–19] In 1985, a ceramic method (CM) strategy was developed, taking a mixture of copper (II) sulfate pentahydrate, potassium bisulfate, and copper (II) chloride dihydrate and heating first to a temperature of 150 ºC for 2 h, then to 600 ºC for 5 h, and finally allowing for a 12 h cooling period. The yielded sample was a powered mixture of needle-like dolerophanite and $K_4[Cu_2O(SO_4)_2]_2 \bullet KCl$ crystals.[14]

In 2019, a chemical vapor transport (CVT) strategy was reported for the synthesis of single-crystal dolerophanite. Volatizing pellets of anhydrous copper (II) sulfate mixed with copper (II) oxide in the presence of the transport agent, gaseous tellurium tetrachloride, yielded a mixture of translucent brown dolerophanite crystals and transparent colorless anhydrous copper (II) sulfate crystals which were then separated by hand through the aid of an optical microscope.[16] A second single-crystal CVT strategy was reported in 2020 by volatizing a mixture of powdered dolerophanite (synthesized via thermal decomposition of copper (II) sulfate as previously described) and nickel (II) bromide in the presence of the transport agent, chlorine gas, yielding semi-transparent brown dolerophanite crystals.[20]

Lastly, in 2020, a composite of dolerophanite and hematite α-Fe_2O_3 was prepared via hydrothermal synthesis (HS) by heating an aqueous suspension containing copper (II) chloride, iron (II) chloride, ethylene glycol, and thiourea hydrothermally at 200 ºC for 20 h under a vacuum in a steel autoclave. The HS product was then treated and allowed to undergo calcination in a muffle furnace at 550 ºC for 2 h, yielding a dark red powder sample.[21]

1.4 Electronic Properties of Dolerophanite

The valency of the copper atoms in dolerophanite was determined in 2019 through X-ray absorption spectroscopy (XAS) at the Cu-L_3 edge.[16] Copper (I) oxide was used as the reference species for the $2p^5 3d^{10} 4s^1$ final electron state of Cu^+ cations and yielded a peak absorbance corresponding to a photon energy of ~932.5 eV. Copper (II) oxide was used as the reference species for the $2p^5 3d^{10}$ final electron state of Cu^{2+} cations and yielded a peak absorbance corresponding to a photon energy of ~930.0 eV.[22]

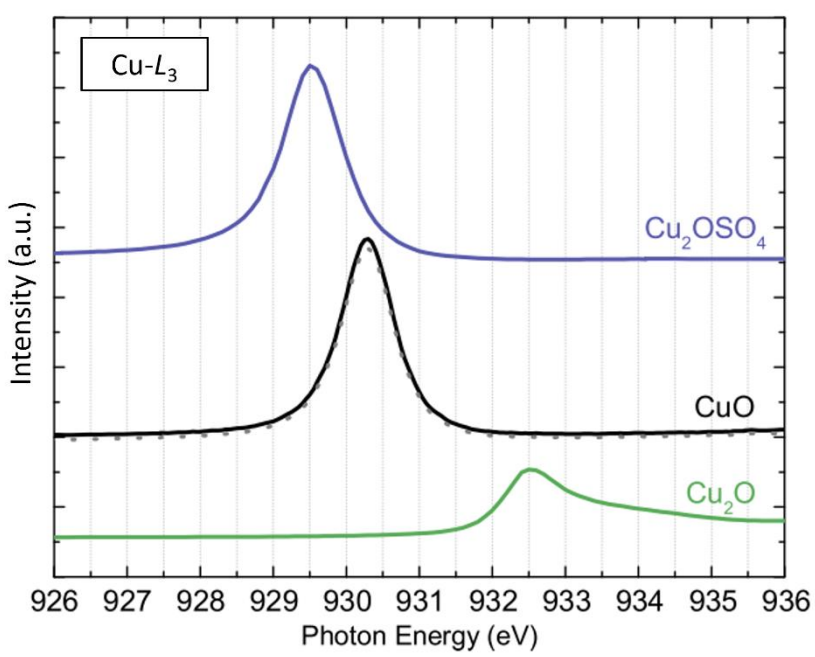

Figure 1-2: XAS taken at the Cu-L_3 edge; adapted from ref 16.

The XAS signature of dolerophanite was found to be at ~929.3 eV, suggesting that the copper atoms are in a divalent state (Figure 1-2); the observed red-shift of the peak absorbance of dolerophanite with respect to copper (II) oxide (Figure 1-2) was attributed to the shorter Cu–O bond length in copper (II) oxide. The Cu–O average bond distance is 1.9543 Å in copper (II) oxide and is 2.170 Å and 2.0306 Å for the Cu1 and Cu2 atom sites, respectively, in dolerophanite.[8]

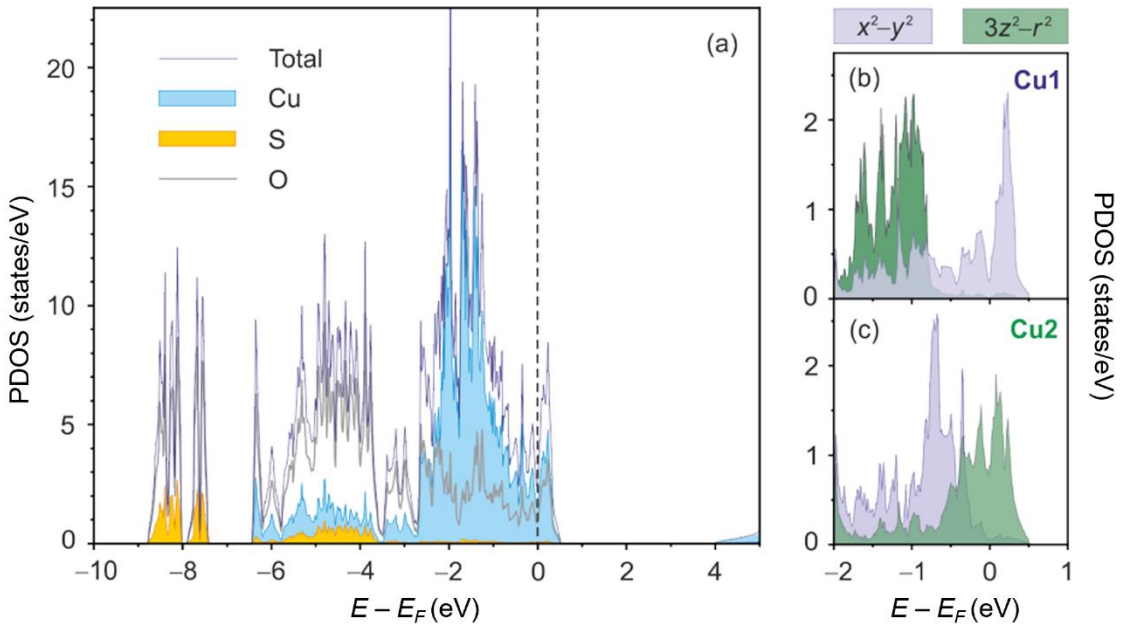

Figure 1-3: Calculated PDOS of dolerophanite with significant copper 3*d* character at the Fermi level, indicated by the dashed line at 0 eV; adapted from ref 23.

Density functional theory (DFT) calculations for the projected density of states (PDOS) were carried out in 2023 using the Perdew–Burke–Ernzerhof functional (PBE) formalism of the exchange-energy potential.[23] These data suggested that the band structure of dolerophanite is metallic in nature and that the most dominant states near the Fermi level were the half-filled $3d_{x^2-y^2}$ state of the Cu1 atom site and the half-filled $3d_{3z^2-r^2}$ state of the Cu2 atom site (Figure 1-3b and 1-3c, respectively). These data further suggested that the 2*p* state of the O atoms was a major contributor to the overall PDOS; in contrast, the 3*p* state of the S atoms contributed little to the overall PDOS (Figure 1-3a).

1.5 Physical Properties of Dolerophanite

The moisture sensitivity and hydration processes of dolerophanite have been extensively studied. In 1961, a mineral called vernadksite was shown to actually be a pseudo-polymorph of antlerite (Atl) $Cu_3(SO_4)(OH)_4$ formed via the following hydration reaction (Equation 1.1) of

dolerophanite crystals in Vesuvius.[12] This was shown by allowing dolerophanite crystals to be heated in an oven at 80 ºC either submerged in distilled water for 12 h or exposed to a humid atmosphere for an entire day; the initial dolerophanite samples were entirely converted to antlerite in this manner as confirmed by pXRD.

$$2Cu_2OSO_4 + 2H_2O \rightarrow Cu_3(SO_4)(OH)_4 + CuSO_4 \quad (1.1)$$

Other hydration processes were then discovered in 2021 by allowing dolerophanite samples to sit open to atmospheres of different relative humidities (RHs) for different durations.[4] It was found that at room temperature, exposure to an atmosphere with at least 85% RH caused dolerophanite to begin undergoing decomposition via the following hydration reaction (Equation 1.2) forming kobyashevite (Kby) $Cu_5(SO_4)_2(OH)_6 \cdot 4H_2O$ and chalcanthite (Cct) $CuSO_4 \cdot 5H_2O$.

$$3Cu_2OSO_4 + 14H_2O \rightarrow Cu_5(SO_4)_2(OH)_6 \cdot 4H_2O + CuSO_4 \cdot 5H_2O \quad (1.2)$$

After only 30 min in an atmosphere with 91% RH, dolerophanite decomposed almost entirely with only 3 wt % remaining; at this point, kobyashevite was the dominant phase at 67 wt % and chalcanthite was the secondary dominant phase at 30 wt %. After 14 h in an atmosphere with 94% RH, dolerophanite decomposed entirely, leaving 67 wt % kobyashevite, 27 wt % antlerite, and 6 wt % chalcanthite. A summary of this evolution of dolerophanite when exposed to moisture is given in Table 1-2. Dehydrating the hydrated samples via heating allowed dolerophanite to reform starting at 325 ºC, but it remained a minor phase at only 20 wt %; this

process yielded a sample with an approximately 70 wt % chalcocyanite $CuSO_2$ major phase and an approximately 10 wt % tenorite CuO minor phase.

Table 1-2: Decomposition of powdered dolerophanite to hydrated copper sulfates. Major phases (≥ 20 wt %) are marked in bold; adapted from ref 4.

85% humidity, 30 min	88% humidity, 60 min	90% humidity, 120 min	91% humidity, 30 min	94% humidity, 14 h
Dph 47 wt %	**Kby 58 wt %**	**Kby 67 wt %**	**Kby 67 wt %**	**Kby 67 wt %**
Kby 28 wt %	**Cct 29 wt %**	**Cct 30 wt %**	**Cct 30 wt %**	**Atl 27 wt %**
Cct 25 wt %	Dph wt %	Dph 3 wt %	Dph 3 wt %	Cct 6 wt %

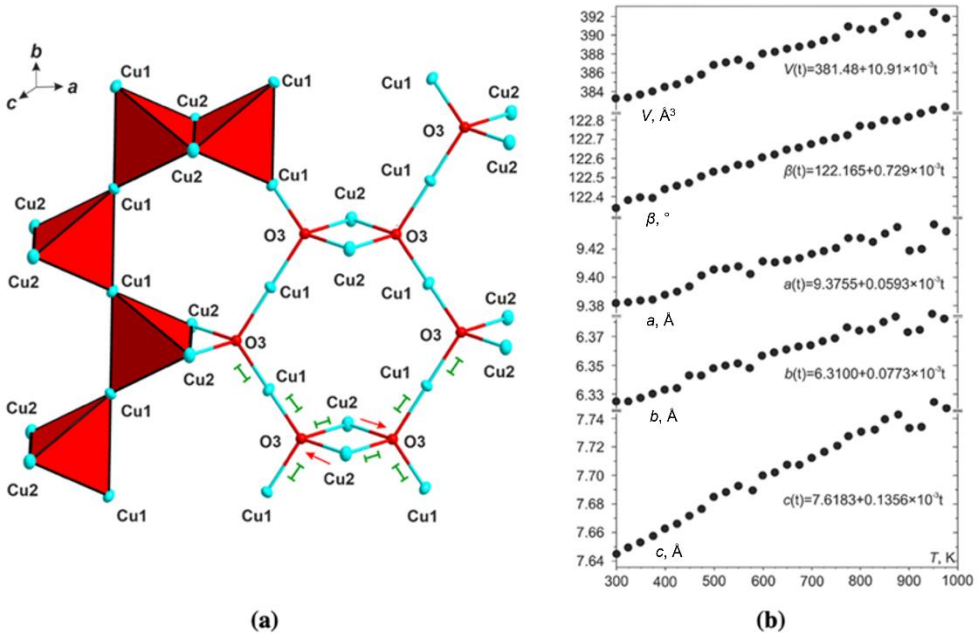

Figure 1-4: (a) Dolerophanite "backbone" with bonds experiencing thermal expansion indicated with red arrows and bonds remaining unchanged during heating indicated with green bars; (b) thermal expansion coefficients as a function of temperature; adapted from ref 8.

The thermal properties of dolerophanite have also been briefly explored. In 2023, polythermal single-crystal XRD was used to explore the thermal expansion and thermal decomposition of dolerophanite.[8] It was found that dolerophanite thermally expanded anisotropically in the *ac*- and *ab*-planes along the copper "backbone"; this was attributed to the

idea that the backbones underwent a thermally-driven shift parallel to one another (Figure 1-4a). When examining the expansions along the lattice parameters (Figure 1-4b), the observed discontinuities in eigenvalues at ~925 °C were attributed to a melting phase transition and it was noted that the known rigidity of the sulfate tetrahedra was likely responsible for the lack of phase transitions before this point.

1.6 Magnetic Properties of Dolerophanite

The magnetic properties of dolerophanite have been a hot topic in the most recent literature regarding the material. This is because dolerophanite is similar to a class of materials referred to as Kagome lattice antiferromagnets.[24]

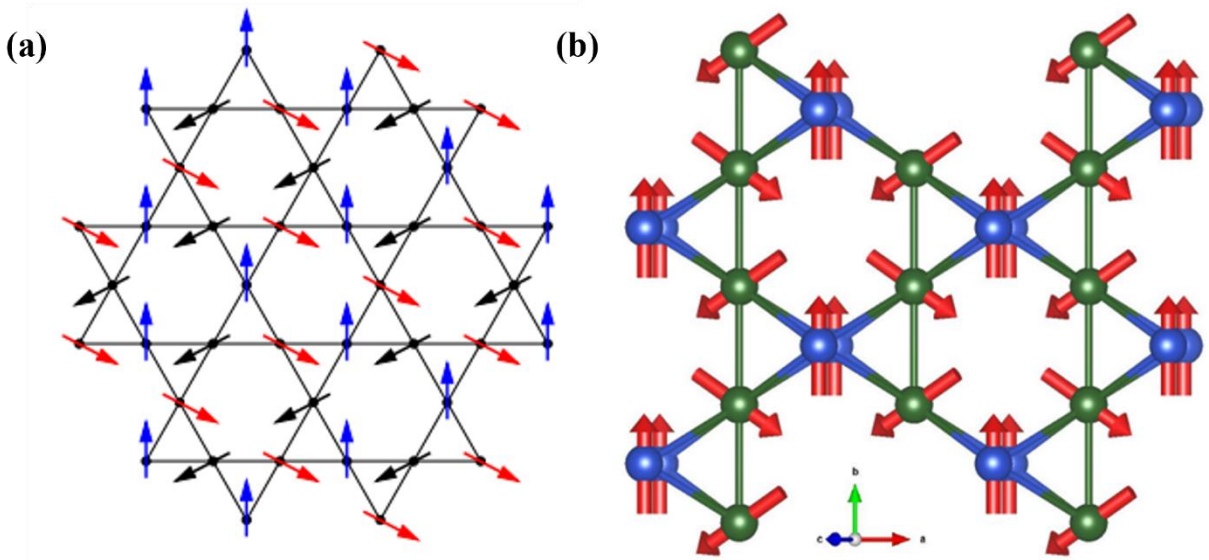

Figure 1-5: (a) Traditional Kagome magnetic structure, from ref 24; (b) Kagome-like magnetic structure indicating the spins of the Cu1 (green) and Cu2 (blue) atom sites; from ref 20.

Named for the traditional Japanese basket-weaving pattern which these layered structures resemble, these $S = 1/2$ systems have antiparallel-aligned spins and thus are considered to be highly "frustrated" due their inability to minimize energy further by rearranging magnetic moment

orientations.[24–26] Dolerophanite is not a true Kagome lattice (Figure 1-5a); instead it is Kagome-*like* in which one third of the spins in a Kagome lattice is replaced by a pair of paramagnetic dimers (Figure 1-5b).[23]

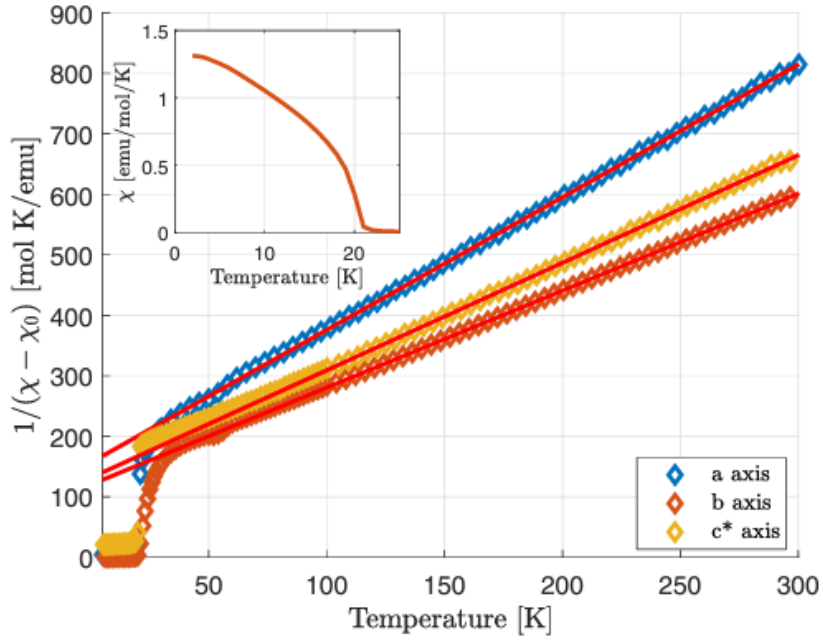

Figure 1-6: Curie–Weiss law fit of dolerophanite magnetic susceptibility along its lattice axes. Data indicate antiferromagnetism above the Curie temperature and weak ferromagnetism below the Curie temperature; from ref 20.

In 2007, it was found that dolerophanite follows the Curie–Weiss law, displaying antiferromagnetic behavior along all lattice axes above a Curie temperature of $T_N = 20$ K and weak ferromagnetism along all lattice axes below the Curie temperature (Figure 1-6);[27] this was corroborated by antiferromagnetic resonance (AFMR) measurements in 2012. AFMR also showed that the spin states of the copper dimers in the *ab*-plane along the "backbone" experienced an antisymmetric exchange interaction known as the Dzyaloshinkii–Moriya (DM) interacton; the DM interaction appears in the Hamiltonian between the two spin states (Equation 1.3). It was determined through AFMR that the D term of the interaction is $D = 6.98 \pm 0.01$ K, indicative of the system exhibiting long-range antiferromagnetic behavior.[18]

$$\mathrm{H} = D \cdot \left(\vec{S}_1 \times \vec{S}_1\right) \tag{1.3}$$

In 2020, neutron diffraction was used to better understand the magnetic structure of dolerophanite; it was found that along the *ab*-plane the material exhibits a 120° magnetic structured ground state.[20] Computational studies have been performed to support the most current experimental data and have also given insight into possible re-orientation phase transitions driven by an imbalance between the antisymmetric and symmetric components of the observed exchange anisotropy.[23]

1.7 Applications of Dolerophanite

Because of the high operating voltage predicted for the $Cu^{2+/3+}$ redox couple, dolerophanite was used to synthesize a lithium-ion battery electrode with composition $Li_2Cu_2O(SO_4)_2$; this was achieved via CM by combining dolerophanite and lithium sulfate powders and annealing them in an inert atmosphere at 500 °C for five days.[19] Through cyclic voltammetry (CV), the resulting electrode showed reversible redox activity at 4.7 V vs. the $Li^{+/0}$ reference electrode (RE) for the $Cu^{2+/3+}$ couple and at 2.5 V vs. $Li^{+/0}$ RE for the $Cu^{2+/0}$ couple. These data underline the possibility of high energy density copper-based electrodes.

Hematite-dolerophanite composites with varying copper-to-iron molar ratios have been synthesized and their ability to degrade Orange II dye via a pseudo-first order photo-Fenton reaction was measured to understand the photocatalytic ability of the composite and its constituents.[21] It was found that while both hematite and dolerophanite do indeed display photocatalytic ability, their degradation rate constants are small, with values of $k = 0.0645$ min^{-1} and $k = 0.0282$ min^{-1}, respectively. The hematite-dolerophanite composite with a copper-to-iron molar ratio of 1:9 (sample referred to as $Cu_2O(SO_4)$-Fe9) displayed substantially greater photo-

Fenton degradation with a rate constant of $k = 0.2627$ min^{-1}, which was 4.07 and 9.33 times greater than hematite and dolerophanite, respectively (Figure 1-7). However, the composites had problems with stability as, over time, there was significant loss of copper (II) cations, necessitating the need for further study of this type of material.

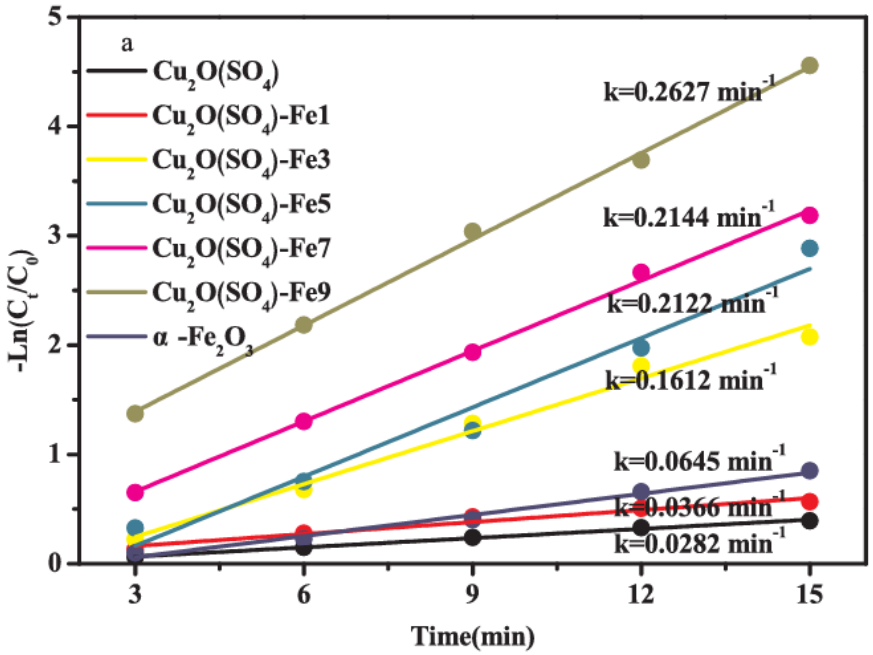

Figure 1-7: Pseudo-first order photo-Fenton degradation of Orange II dye by hematite, dolerophanite, and hematite-dolerophanite composites with varying Cu:Fe ratios; from ref 21.

1.8 Solution Combustion Synthesis

Solution combustion synthesis (SCS) is a method for synthesizing nanoscale solid-state materials by allowing a precursor solution to undergo a self-sustained combustion reaction. Metal oxides can be readily synthesized by SCS by utilizing metal nitrates or metal nitrate hydrates as the oxidizer precursor and an organic fuel such as urea or malic acid as the fuel in an aqueous solution.[28] While in solution, the precursors are mixed at the molecular level as opposed to CM in which powders are mixed only at the micro level. The precursor solution is placed into a pre-heated

furnace, typically between 300 ºC and 500 ºC, at which point dehydration of the solution, formation and decomposition of a reaction gel, and self-ignition and combustion of the gel occur in a single step. The SCS product can be further refined via annealing to remove any carbonaceous species.[29]

During the combustion, it has been observed that as the reaction mixture burns, it produces a flame which can reach a maximum temperature of ~1350 ºC, and the mixture releases a large amount of gaseous byproducts, namely nitrogen, carbon dioxide, and water. This release of gas allows the SCS product to expand and rapidly cool, leading to a well-dispersed porous powder sample.[30]

While metal oxides are a primary focus of SCS, the synthesis of metal sulfides (most notably cadmium (II) sulfide, zinc sulfide, and various nickel sulfides) has been demonstrated by utilizing a sulfur-containing organic fuel such as thiourea or thiosemicarbozide.[31–33]

Due to SCS being both time- and energy-efficient compared to more traditional solid-state synthesis strategies, the Rajeshwar group has been interested in utilizing SCS to produce semiconductors for the purpose of solar water splitting.[28, 34–36] Using the ternary Cu–V–O and Mg–V–O families as case studies, it has been shown that, in addition to this efficiency, SCS has the capability of providing a quick way to survey various compositions and polymorphs in a compound family by tuning both the precursor molar ratios and the post-process annealing.[34] It has also been shown that SCS has the capability to achieve phase-pure samples that are difficult to produce with traditional strategies.[35] Lastly, it is possible to use SCS to produce composition-controlled solid-solutions which, in turn, can have an impact on optical bandgap engineering.[36] This demonstrates the flexibility of SCS as a tool in the tuning of materials properties.

1.9 Final Remarks

Dolerophanite is an interesting material due in part to its complex structure and its magnetic properties; and yet, despite interest in the material, there are clear gaps in the available literature due to the rarity of the material and its instability to high temperature and humidity conditions. Synthesis strategies for bulk dolerophanite are limited to slow traditional solid-state strategies such as the CM pathway. There is need for more efficient synthesis strategies and for further characterization of the material. As such, this work aims to demonstrate a novel SCS pathway for dolerophanite and provide characterization on the material that may help further the understanding of its optical and thermal properties.

1.10 References

(1) Pautov, L. A.; Mirakov, M. A.; Siidra, O. I.; Faiziev, A. R.; Nazarchuk, E. V.; Kaprenko, V. Y.; Mahkmadsharif, S. Flagarite, $K_4(VO)_3(SO_4)_5$, a New Mineral from Sublimates of a Natural Underground Coal Fire at the Tract of Kukhi-Malik, Fan-Yagnob Coal Deposit, Tajikistan. *Mineral. Mag.* **2020**, *84*, 455–462.

(2) Bergerhoff, G.; Paeslack, J. Sauerstoff als Koordinationszentrum in Kristallstrukturen. *Z. Kristallogr.* **1968**, *126*, 112–123.

(3) Krivovichev, S. V.; Filatov, S. K.; Semenova, T. F. Types of cationic Complexes Based on Oxocentered Tetrahedra $[OM_4]$ in the Crystal Structures of Inorganic Compounds. *Russ. Chem. Rev.* **1998**, *67*, 137–155.

(4) Siidra O. I.; Borisov, A. S.; Charkin, D. O.; Depmeier, W.; Platonova, N. V. Evolution of Fumarolic Anhydrous Copper Sulfate Minerals During Successive Hydration/Dehydration. *Mineral. Mag.* **2021**, *85*, 262–277.

(5) Krivovichev, S. V.; Mentré, O.; Siidra, O. I.; Colmont, M.; Filatov, S. K. Anion-Centered Tetrahedra in Inorganic Compounds. *Chem. Rev.* **2013**, *113,* 6459–6535.

(6) Balassone, G.; Petti, C.; Mondillo, N.; Panikorovskii, T. L.; de Gennaro, R.; Cappelletti, P.; Altomare, A.; Corriero, N.; Cangiano, M.; D'Orazio L. Copper Minerals at Vesuvius Volcano (Southern Italy): A Mineralogical Review. *Minerals* **2019**, *9*, 730.

(7) Pekov, I. V.; Zubkova, N. V.; Pushcharovsky, D. Y. Copper Minerals from Volcanic Exhalations – A Unique Family of Natural Compounds: Crystal-Chemical Review. *Acta. Cryst.* **2018**, *74*, 502–518.

(8) Nazarchuk, E. V.; Siidra, O. I.; Filatov, S. K.; Charkin, D. O.; Zhdanova, L. R. Thermal Expansion of Anhydrous Copper Sulfate Minerals Determined by Single Crystal X-Ray Diffraction: Chalcocyanite $CuSO_4$, Dolerophanite Cu_2OSO_4 and Kamchatkite $KCu_3O(SO_4)_2Cl$. *Phys. Chem. Miner.* **2023**, *50*, 11–19.

(9) Warr, L. N. IMA–CNMNC Approved Mineral Symbols. *Mineral. Mag.* **2021**, *85*, 291–320.

(10) Scacci, A. Nuove Specie di Solfati di Rame (Dolerofano). In *Note Mineralogiche, Memoria Prima*; Stamperia del Fibreno: Naples, 1873, pp. 22–29.

(11) Richmond, W. E.; Wolfe, C. W. Crystallography of Dolerophanite. *Am. Min.* **1940**, *25*, 606–610.

(12) Mrose, M. E. Vernadskite Discredited: Pseudomorphs of Antlerite After Dolerophanite. *Am. Min.* **1961**, *46*, 146–154.

(13) Flügel-Kahler, E. Die Kristallstruktur von Dolerophanit, $Cu_2O(SO_4)$. *Acta. Crystallogr.* **1963**, *16*, 1009–1014.

(14) Effenberger, H. $Cu_2O(SO_4)$, Dolerophanite: Refinement of the Crystal Structure, with a Comparison of $[OCu(II)_4]$ Tetrahedra in Inorganic Compounds. *Montash. Chem.* **1985**, *116*, 927–931.

(15) Jacobsen S. D.; Smyth, J. R.; Swope, R. J.; Downs, R. T. Rigid-Body Character of the SO_4 Groups in Clestine, Anglesite and Barite. *Can. Mineral.* **1998**, *36*, 1053–1060.

(16) Zhao, L.; Dalton, C.; Liao, S. C.; Hu, Z.; Lin, H. J.; Chen, C. T. Komarek, A. C. Single Crystal Growth and Physical Properties of Dolerophanite Single Crystals. *Phys Rev. Mater.* **2019**, *3*, 124403.

(17) Binder, O. Definition Des Sulfates Basiques de Cuivre. *Ann. Chim.* **1936**, *5*, 337–409.

(18) Takahashi, N.; Okubo, S.; Ohta, H.; Sakurai, T.; Fujisawa, M.; Kikuchi, H. Dzyaloshinsky-Moriya Interaction Estimated by AFMR of Kagome Like Substance $Cu_2O(SO_4)$ Observed at 1.8K. *J. Phys.: Conf. Ser.* **2012**, *400*, 1–4.

(19) Sun, M.; Rousse, G.; Abakumov, A. M.; Saubanère, M.; Doublet, M.-L.; Jose Rodriguez-Carvajal, J.; Tendeloo, G. Van; Tarascon, J.-M.; Rousse, G.; Dou-Blet, M.-L.; Rodríguez-Carvajal, J.; Van Tendeloo, G. $Li_2Cu_2O(SO_4)_2$: A Possible Electrode for Sustainable Li-Based Batteries Showing a 4.7 V Redox Activity vs. Li^+/Li^o. *Chem. Mater*. **2015**, *27*, 3077–3087.

(20) Favre, V. Y.; Tucker, G. S.; Ritter, C.; Sibille, R.; Manuel, P.; Frontzek, M. D.; Kriener, M.; Yang, L.; Berger, H.; Magrez, A.; Casati, N. P. M.; Zivkovic, I.; Ronnow, H. M. Ferrimagnetic 120° Magnetic Structure in Cu_2OSO_4. *Phys. Rev. B* **2020**, *102*, 094422.

(21) Guo, X.; Xu, Y.; Zha, F.; Tang, X.; Tian, H. α-Fe_2O_3/$Cu_2O(SO_4)$ Composite as a Novel and Efficient Heterogeneous Catalyst for Photo-Fenton Removal of Orange II. *Appl. Surf. Sci.* **2020**, *530*, 147144.

(22) Lee, S. W.; Guo, H.; Zhao, L.; Hu, Z.; Mueller, T.; Lin, H. J.; Chen, C. T.; Ryu, G.; Tjeng, L. H.; Komarek, A. C. $Cu_2M\ SiO_5$ (M = Co, Ni): A New Silicate Material with Chains of Cu and M Ions. *Phys. Rev. Materials* **2019**, *3*, 034408.

(23) Panther, A.; Tsirlin, A.; Rousochatzakis, I. Frustration Relief and Reorientation Transition in the Kagome-Like Dolerophanite Cu_2OSO_4. *Phys. Rev. B* **2023**, *108*, 224410.

(24) Zhitomirsky, M. E. Octupolar Ordering of Classical Kagome Antiferromagnets in Two and Three Dimensions. *Phys. Rev. B* **2008**, *78*, 094423.

(25) Yin, J.-X.; Zhang, S. S.; Li, H.; Jiang, K.; Chang, G.; Zhang, B.; Lian, B.; Xiang, C.; Belopolski, I.; Zheng, H.; Cochran, T. A.; Xu, S.-Y.; Bian, G.; Liu, K.; Chang, T.-R.; Lin, H.; Lu, Z.-Y.; Wang, Z.; Jia, S.; Wang, W.; Hasan, M. Z. Giant and Anisotropic Many-Body Spin–Orbit Tunability in a Strongly Correlated Kagome Magnet. *Nature* **2018**, *562*, 91–95.

(26) Neupert, T.; Denner, M. M.; Yin, J.-X.; Thomale, R.; Hasan, M. Z. Charge Order and Superconductivity in Kagome Materials. *Nat. Phys.* **2021**, *18*, 137–143.

(27) Asano, T.; Ichimura, S.; Nishimura, T.; Wada, H. Low-Dimensionality and Geometrically-Frustrated Effect of $Cu_2O(SO_4)$. *Spring Meeting of Phs. Soc. Jpn.* **2007**, 18aRB-6.

(28) Rajeshwar, K.; de Tacconi, N. R. Solution Combustion Synthesis of Oxide Semiconductors for Solar Energy Conversion and Environmental Remediation. *Chem. Soc. Rev.* **2009**, *38*, 1984–1998.

(29) Varma, A.; Mukasyan, A. S.; Rogachev, A. S.; Manukyan, K. V. Solution Combustion Synthesis of Nanoscale Materials. *Chem. Rev.* **2016**, *116*, 14493–14586.

(30) Patil, K. C.; Hedge, M. S.; Rattan, T.; Aruna, S. T. *Chemistry of Nanocrystalline Oxide Materials: Combustion Synthesis, Properties and Applications*; World Scientific: Singapore, 2008.

(31) Arora, S.; Manoharan, S. S. Size-Dependent Photoluminescent Properties of Uncapped CdS Particles Prepared by Acoustic Wave and Microwave Method. *J. Phys. Chem. Solids* **2007**, *68*, 1897–1901.

(32) Mani, A. D.; Ghosal, P.; Subrahmanyam, C. Novel Synthesis of C, N Doped Rice Grain Shaped ZnS Nanomaterials – Towards Enhanced Visible Light Photocatalytic Activity for Aqueous Pollutant Removal and H_2 Production. *RSC Adv.* **2014**, *4*, 23292–23298.

(33) Mani, A. D.; Deepa, M.; Xanthopoulos, N. Subrahmanyam, C. Novel One Pot Stoichiometric Synthesis of Nickel Sulfide Nanomaterials as Counter Electrodes for QDSSCs. *Mater. Chem. Phys.* **2014**, *148*, 395–402.

(34) Hossain, M. K.; Sotelo, P.; Sarker, H. P.; Galente, M. T.; Kormányos, A.; Longo, C.; Macaluso, R. T.; Huda, M. N.; Janáky, C.; Rajeshwar, K. Rapid One-Pot Synthesis and Photoelectrochemical Properties of Copper Vanadates. *ACS Appl. Energy Mater.* **2019**, *2*, 2837–2847.

(35) Hossain, M. K.; Sarker, H. P.; Sotelo, P.; Dang, U.; Rodríguez-Gutiérrez, I.; Blawat, J.; Vali, A.; Xie, W.; Oskam, G.; Huda, M. N.; Macaluso, R. T.; Rajeshwar, K. Phase-Pure Copper Vanadate (α-CuV_2O_6): Solution Combustion Synthesis and Characterization. *Chem. Mater.* **2020**, *32*, 6247–6255.

(36) Rawat, A.; Clark, L.; Zhang, C.; Cavin, J.; Sangwan, V. K.; Toth, P. S.; Janáky, C.; Ananth, R.; Goldfine, E.; Bedzyk, M. J.; Weiss, E. A.; Rondinelli, J. M.; Hersam, M. C.; Meletis, E. I.; Rajeshwar, K. Solution Combustion Synthesis and Characterization of Magnesium Copper Vanadates. *Inorg. Chem.* **2023**, *62*, 8903–8913.

CHAPTER 2: EXPERIMENTAL AND THEORETICAL METHODS

2.1 Materials

Copper (II) nitrate hemi(pentahydrate) [$Cu(NO_3) \cdot 2.5H_2O$ (Thermo Scientific)] was utilized as the copper source and thiourea [$SC(NH_2)_2$ (J. T. Baker)] was utilized as both the sulfur source and the fuel in the solution combustion synthesis (SCS). Anhydrous copper (II) sulfate [$CuSO_4$ (Alfa Aesar)] was used as the starting reagent in the ceramic method (CM) synthesis. All reagents were used as received from their respective commercial sources without any additional purification.

2.2 Synthesis

SCS was performed by combining aqueous 0.25 M copper (II) sulfate hemi(pentahydrate) and 0.25 M thiourea to obtain an oxidant-to-fuel ratio of 1:1. This mixture was allowed to homogenize via sonication bath, yielding a precursor solution light-blue in color. The precursor solution was then placed in a preheated muffle furnace at ~315 ºC for 15 min to allow for dehydration and ignition. The resulting yellow-grey "crude" sample was then ground into a fine powder and transferred to an alumina crucible to allow for post-SCS processing and cleanup of any remnant carbonizing species. To achieve phase-pure dolerophanite Cu_2OSO_4, the sample was annealed, heating the powder in an alumina crucible in a muffle furnace at a rate of 20 ºC/min from room temperature to 650 ºC, holding at this temperature for 1 h, and cooling back to room temperature at a rate of 20 ºC. The resulting sample (identified as Dph_SCS) was finely powdered

and yellow-grey in color. Typical yield was ~80%. A schematic diagram of the SCS process is shown in Figure 2-1.

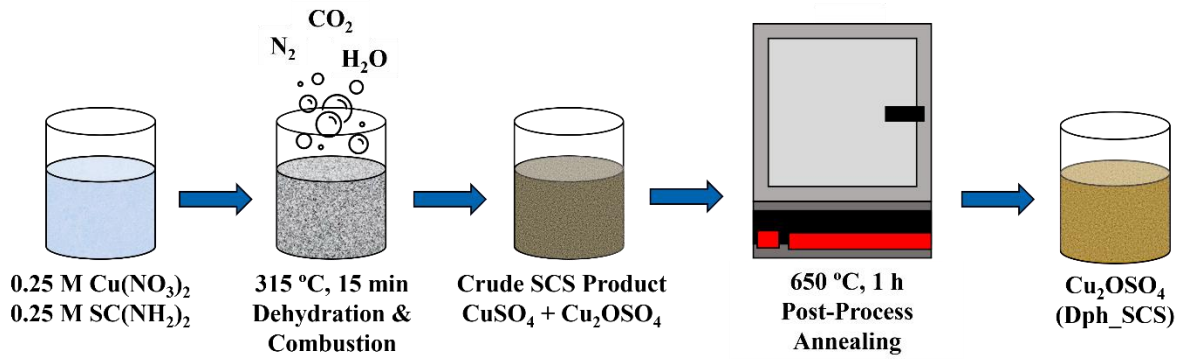

Figure 2-1: Schematic diagram of the SCS pathway for dolerophanite.

To confirm the thermal decomposition product, crude SCS product was also separately annealed from room temperature to a final temperature of 750 ºC, holding at this temperature for 1 h, and cooling back to room temperature, utilizing the same heating and cooling profile as before. A summary of the impact of the annealing profile is shown in Figure 2-2. Additional details concerning SCS can be found in ref 1–3.

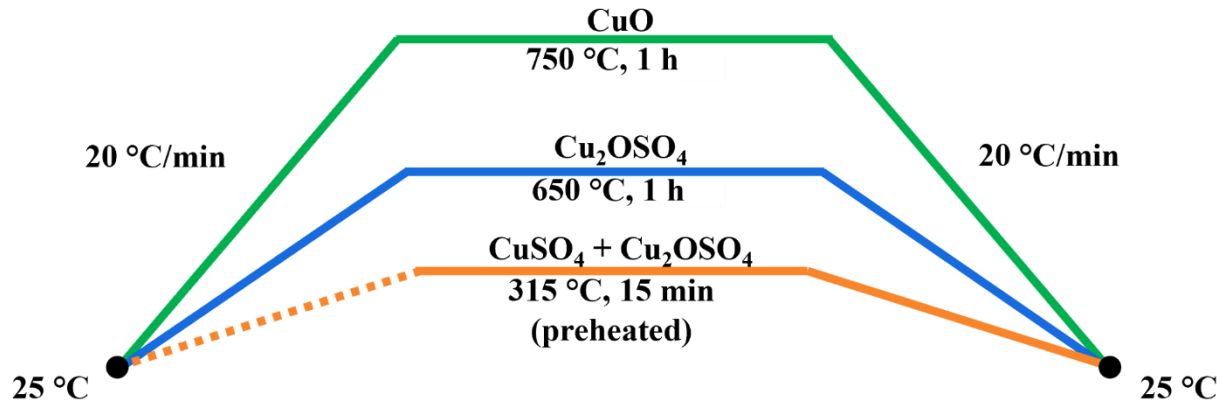

Figure 2-2: Schematic diagram of the impact of annealing profile on SCS product.

CM synthesis was performed by annealing blueish-white finely powdered anhydrous copper (II) sulfate in an alumina crucible in a muffle furnace from room temperature to 650 ºC,

holding at this temperature for 1.5 h, and cooling back to room temperature, utilizing the same heating and cooling profile as before. The resulting sample (identified as Dph_CM) was finely powdered and yellow in color. Typical yield was ~98%. A schematic diagram of the CM process is shown in Figure 2-3. Additional details concerning this synthesis pathway can be found in ref 4 and 5. Synthesis of both Dph_SCS and Dph_CM was carried out with the help of Vaishnavi Guttikonda from the Rajeshwar group.

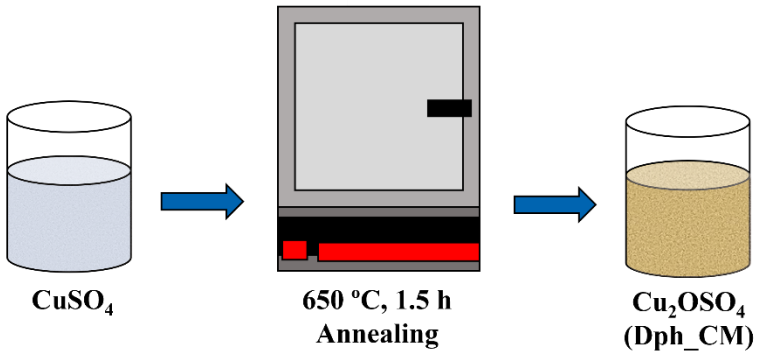

Figure 2-3: Schematic diagram of the CM pathway for dolerophanite.

2.3 Physical Characterization

Powder X-ray diffraction (pXRD) measurements were performed on a Bruker D8 Advanced X-ray diffractometer. It was equipped with a LYNXEYE XE-T detector operated in the 1D mode. Diffraction patterns were collected using para-focusing Bragg-Brentano θ/2θ geometry over a 2θ range of 20º–60º at a scan speed of 0.25º 2θ/min and 0.03º step size. Rietveld refinement of the diffraction patterns was performed using the GSAS-II open-source crystallography software package.[6] Open-sourced Visualization for Electronic and Structural Analysis (VESTA) software was utilized for the visualization of refined crystal structures.[7]

Scanning electron microscopy (SEM) and energy-dispersive X-ray spectroscopy (EDX) were performed on a Hitachi S-3000N variable pressure scanning electron microscope with a tungsten electron source and an attached NORAN 7 Integrated EDX/EBSD system. SEM-EDX and refinement were performed with the help of Abhishek Rawat and Katheryn Cruz from the Rajeshwar group. Selected area electron diffraction (SAED) and transmission electron microscopy (TEM) were performed on a Hitachi H-9500 high-resolution transmission electron microscope with an accelerated voltage of 300 kV with an attached 4008 x 2672-pixel SC-1000 Orius TEM CCD camera. TEM-SAED was carried out by Chuzhong Zhang from the Meletis group.

2.4 Thermal Analysis

Thermogravimetric analysis (TGA) and differential scanning calorimetry (DSC) were performed using a Discovery SDT 650 simultaneous thermal analyzer. Thermal analysis was performed on the temperature range of 25.00 ºC–1000.00 ºC with heating rates, β, ranging 2.00 ºC/min–25.00 ºC/min under constant 50.00 mL/min nitrogen gas flow.

Activation energy, E_a, was estimated using the Kissinger equation (Equation 2.1),[8, 9] assuming first-order reaction kinetics.

$$\ln\left(\frac{\beta}{T_p^2}\right) = \ln\left(\frac{-AR}{E_a} f'(\alpha)\right) - \frac{E_a}{RT_p} \tag{2.1}$$

Here, R is the ideal gas constant, T_p is the temperature of rate peak maximum, A is the Arrhenius preexponential factor, and $f'(\alpha)$ is a function corresponding to the reaction model.[9–10]

2.5 Spectroscopic Analysis

Fourier transform infrared spectroscopy (FTIR) was performed on a Bruker Alpha-P attenuated total reflectance (ATR) FTIR spectrophotometer. Raman spectroscopy was performed on a Thermo Scientific DXR 3 Raman microscope equipped with a 532 nm laser operated at 2.0 mW power.

Ultraviolet-visible spectroscopy (UV-vis) and diffuse reflectance spectroscopy (DRS) was performed on a Shimadzu UV-3600 spectrophotometer. The reflectance data were analyzed to predict the optical bandgap, E_g, of the material. This was done by determining the Kubelka–Munk function (Equation 2.2) of the reflectance R_∞ of an infinitely thick sample where a and s are the absorption and scattering coefficients, respectively.[11]

$$F(R_\infty) = \frac{a}{s} = \frac{(1 - R_\infty)^2}{2R_\infty} \tag{2.2}$$

The Kubelka-Munk function then served as the absorption coefficient in the Tauc equation (Equation 2.3).[12]

$$(F(R_\infty) \cdot h\nu)^{1/\gamma} = B \cdot (h\nu - E_g) \tag{2.3}$$

Here, h is the Planck constant, ν is the frequency of incident light, B is an arbitrary constant, and γ is equal to 1/2 or 2 for direct and indirect bandgap optical transitions, respectively. For semiconductor materials, the plot of the Tauc equation exhibits a characteristic sharp linear increase of the reflectance term which, when extrapolated to the baseline of the curve, provides an estimate of the optical bandgap, E_g.[13]

2.6 Computational Methodology

Density functional theory (DFT) calculations were carried out on Quantum Espresso open-source software.[14] Calculations were carried out using the revised Perdew–Burke–Ernzerhof functional for solids (PBEsol) formalism of the generalized gradient approximation (GGA)[15] and the projector augmented-wave (PAW) potential.[16] An unshifted k-point mesh of 4 x 6 x 6 was used for the calculations on bulk dolerophanite; a dense k-mesh grid of 8 x 12 x 12 was used for the density of state (DOS) calculations; a high-symmetry k-path was used for band calculations. An 85 Ry/750 Ry cutoff energy was chosen for the plane wave basis set. Parameters were benchmarked with respect to the experimental lattice parameters of bulk system dolerophanite.

Semi-local van der Waals calculations were not considered in the calculations. A comparison of bulk lattice parameters calculations was performed via DFT both with and without Hubbard U and exchange coupling J parameters. A Heyd–Scuseria–Ernzerhof hybrid functional (HSE) was also performed along with collinear magnetic calculations.

All calculations were carried out by Dr. Abhishek Kumar Adak from The Abdus Salam International Centre for Theoretical Physics in Trieste, Italy.

2.7 References

(1) Hossain, M. K.; Sotelo, P.; Sarker, H. P.; Galente, M. T.; Kormányos, A.; Longo, C.; Macaluso, R. T.; Huda, M. N.; Janáky, C.; Rajeshwar, K. Rapid One-Pot Synthesis and Photoelectrochemical Properties of Copper Vanadates. *ACS Appl. Energy Mater.* **2019**, *2*, 2837–2847.

(2) Hossain, M. K.; Sarker, H. P.; Sotelo, P.; Dang, U.; Rodríguez-Gutiérrez, I.; Blawat, J.; Vali, A.; Xie, W.; Oskam, G.; Huda, M. N.; Macaluso, R. T.; Rajeshwar, K. Phase-Pure Copper Vanadate (α-CuV_2O_6): Solution Combustion Synthesis and Characterization. *Chem. Mater.* **2020**, *32*, 6247–6255.

(3) Rawat, A.; Clark, L.; Zhang, C.; Cavin, J.; Sangwan, V. K.; Toth, P. S.; Janáky, C.; Ananth, R.; Goldfine, E.; Bedzyk, M. J.; Weiss, E. A.; Rondinelli, J. M.; Hersam, M. C.; Meletis, E. I.; Rajeshwar, K. Solution Combustion Synthesis and Characterization of Magnesium Copper Vanadates. *Inorg. Chem.* **2023**, *62*, 8903–8913.

(4) Binder, O. Definition Des Sulfates Basiques de Cuivre. *Ann. Chim.* **1936**, *5*, 337–409.

(5) Mrose, M. E. Vernadskite Discredited: Pseudomorphs of Antlerite After Dolerophanite. *Am. Min.* **1961**, *46*, 146–154.

(6) Toby, B. H.; Von Dreele, R. B. GSAS-II: The Genesis of a Modern Open-Source All Purpose Crystallography Software Package. *J. Appl. Cryst.* **2013**, *46*, 544–549.

(7) Momma, K.; Izumi, F. VESTA 3 for Three-Dimensional Visualization of Crystal, Volumetric and Morphology Data. *J. Appl. Crystallogr.* **2011**, *44*, 1272–1276.

(7) Kissinger, H. E. Variation of Peak Temperature with Heating Rate in Differential Thermal Analysis. *J. Res. Natl. Bur. Stand.* **1956**, *57*, 217–221.

(8) Kissinger, H. E. Reaction Kinetics in Differential Thermal Analysis. *Anal. Chem.* **1957**, *29*, 1702–1706.

(9) Vyazovkin, S.; Burnham, A. K.; Criado, J. M.; Pérez-Maqueda, L. A.; Popescu, C.; Sbirrazzuoli, N. ICTAC Kinetics Committee Recommendations for Performing Kinetic Compuations on Thermal Analysis Data. *Thermochim. Acta* **2011**, *520*, 1–19.

(10) Kubelka, P.; Munk, F. An Article on Optics of Pain Layers. *Z. Techn. Phys.* **1931**, *12*, 593–599.

(11) Tauc, J.; Grigorovici, R.; Vancu, A. Optical Properties and Electronic Structure of Amorphous Germanium. *Phys. Status Solidi B* **1966**, *15*, 627–537.

(12) Makula, P.; Pacia, M.; Macyk, W. How to Correctly Determine the Band Gap Energy of Modified Semiconductor Photocatalysts Based on UV-Vis Spectra. *J. Phys. Chem. Lett.* **2018**, *9*, 6814–6817.

(13) Giannozzi, P.; Baroni, S.; Bonini, N.; Calandra, N.; Car, R.; Cavazzoni, C.; Ceresoli, D.; Chiarotti, G. L.; Cococcioni, M.; Dabo, I.; Dal Corso, A.; de Gironcoli, S.; Fabris, S.; Fratesi, G.; Gebuaer, R.; Gerstmann, U.; Gougoussis, C.; Kokalj, A.; Lazzeri, M.; Martin-Samos, L.; Marzari, N.; Mauri, F.; Mazzarello, R.; Paolini, S.; Pasquarello, A.; Paulatto, L.; Sbraccia, C.; Scandolo, S.; Sclauzero, G.; Seitsonen, A. P.; Smogunov, A.; Umari, P.; Wentzcovitch, R. M. QUANTUM ESPRESSO: A Modular and Open-Source Software Project for Quantum Simulations of Materials. *J. Phys.: Condens. Matter* **2009**, *21*, 395502.

(14) Perdew, J.P.; Burke, K.; Ernzerhof, M. Generalized Gradient Approximation Made Simple. *Phys. Rev. Lett.* **1996**, *77*, 3865–3868.

(15) Blöchl, P. E. Projector Augmented-Wave Method. *Phys. Rev. B* **1994***, 50*, 17953.

(16) Heyd, J.; Scuseria, G. E.; Ernzerhof, M. Hybrid Functionals Based on a Screened Coulomb Potential. *J. Chem. Phys.* **2003**, *118*, 8207–8215.

CHAPTER 3: RESULTS AND DISCUSSION

3.1 Physical Characterization

The yield for solution combustion synthesis (SCS) of dolerophanite Cu_2OSO_4 (sample identified as Dph_SCS) from copper (II) nitrate hemi(pentahydrate) was ~80%, calculated using a 2:1 precursor-to-product molar ratio based on the proposed reaction (Equation 3.1).[1] The yield for the ceramic method (CM) synthesis of dolerophanite (sample identified as Dph_CM) from anhydrous copper (II) sulfate was ~98%, calculated using a 2:1 precursor-to-product molar ratio based on the proposed reaction (Equation 3.2).[2] The yields for both product samples are summarized in Table 3-1.

$$2Cu(NO_3)_2 \cdot 2.5H_2O(aq) + 2SC(NH_2)_2 + 2O_2(g) \rightarrow Cu_2OSO_4(s) + SO_3(g) + 4N_2(g) + 2CO_2(g) + 9H_2O(g) \quad (3.1)$$

$$2CuSO_4(s) \xrightarrow{\Delta} Cu_2OSO_4(s) + SO_3(g) \quad (3.2)$$

Table 3-1: Yields for SCS and CM pathways for dolerophanite.

Sample	Molar Mass (g/mol)	Theoretical Yield (mg)	Actual Yield (mg)	%Yield
Dph_SCS	239.154	597.9	478.0	79.9
Dph_CM	239.154	825.3	804.7	97.5

The powder X-ray diffraction (pXRD) spectra of both samples (Figure 3-1a) indicated crystallization in the *C*2/*m* space group, consistent with the known structure (Figure 3-1b). Qualitatively, the spectra indicated that both samples display good crystallinity and are phase-pure; trace impurity, if any, would come from anhydrous copper (II) sulfate, indicative of an insufficient annealing. Reference spectra for copper (II) oxide sulfate and copper (II) were taken from ref 3 and 4, respectively.

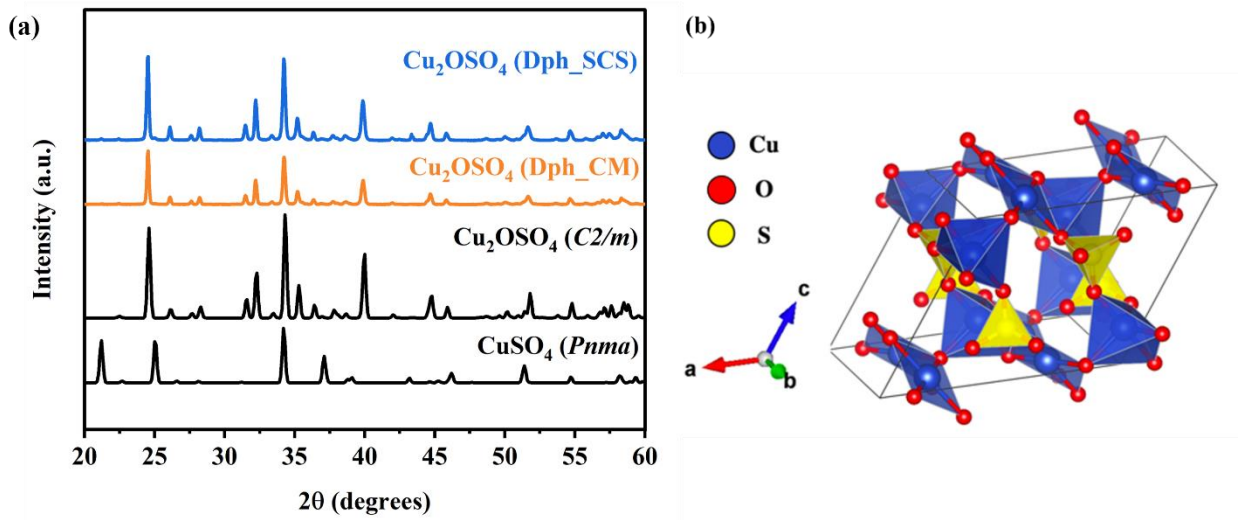

Figure 3-1: (a) pXRD spectra for Dph_SCS and Dph_CM; (b) monoclinic *C*2/*m* crystal structure of the refined diffraction pattern of Dph_SCS, visualized through VESTA software. Reference spectra taken from ref 3 and 4.

Table 3-2: Lattice parameters of Dph_SCS and Dph_CM obtained from Rietveld refinement of the pXRD data.

Sample	*a* (Å)	*b* (Å)	*c* (Å)	*α* (°)	*β* (°)	*γ* (°)	*V*(Å^3)	R_{wp} (%)
Dph_SCS	9.39268	6.33669	7.66604	90.000	122.407	90.000	385.211	18.16
Dph_CM	9.39229	6.33434	7.66131	90.000	122.385	90.000	384.910	18.45
Ref 3	9.370	6.319	7.639	90.00	122.34	90.00	382.1	—
Ref 5	9.3993	6.3391	7.6688	90.00	122.434	90.00	385.65	—

Rietveld refinement of the crystal structures indicated excellent agreement between the cell parameters of the experimental samples and reference structures; specifically, differences between samples and references did not exceed 1%. Refinement also indicated that Dph_SCS was slightly

less dense than Dph_CM, as indicated by reported volumes. The weighted profile R-factor (R_{wp}) for both samples was ~18% necessitating the need for further refinement with more sensitive pXRD spectra in the future. A summary of the refined lattice parameters is provided in Table 3-2 and the refined pXRD spectra of both samples are shown in Figure 3-2.

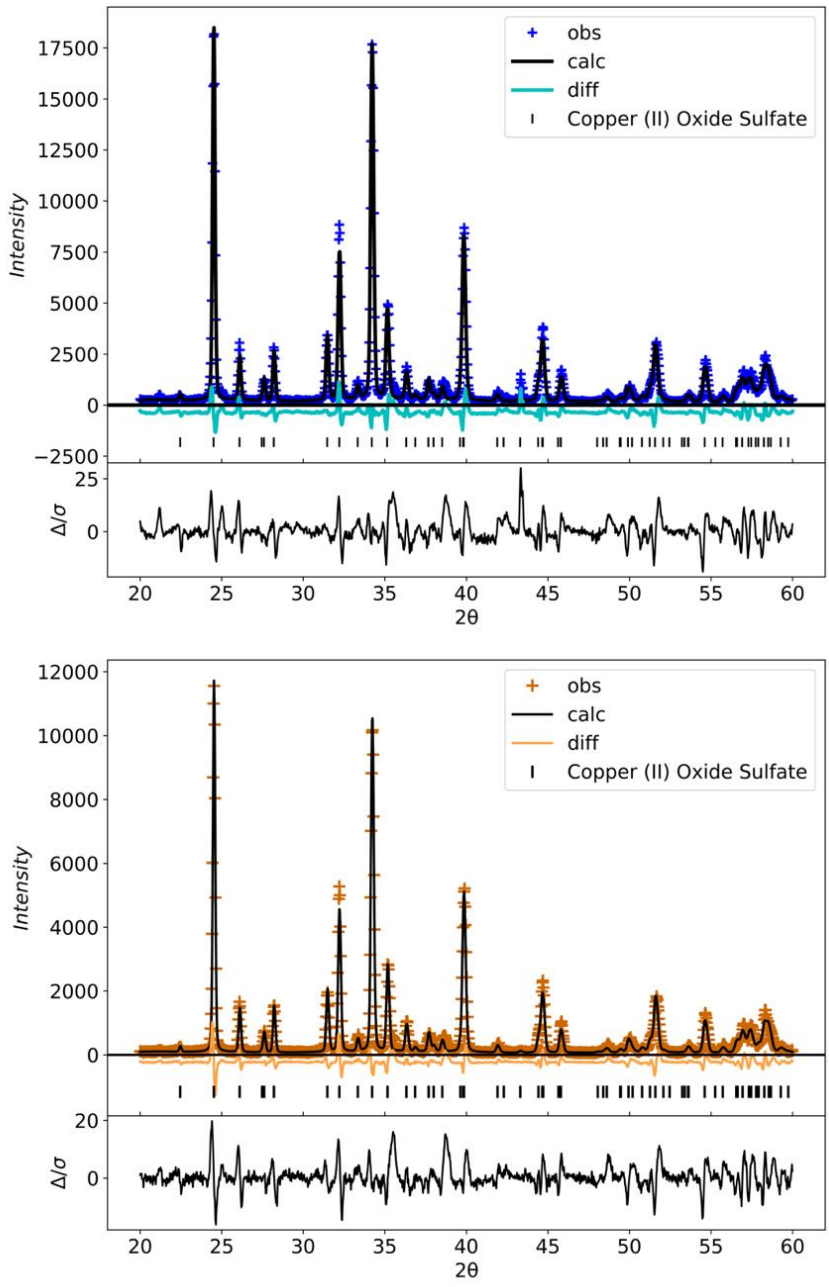

Figure 3-2: Refinement of the pXRD data for Dph_SCS (top) and Dph_CM (bottom).

Comparing the surficial structure of the two dolerophanite samples with both low magnification (Figure 3-3a and 3-3b) and high magnification (Figure 3-3c and 3-3d) scanning electron microscopy (SEM) images provided a striking difference between the products of the two synthesis strategies. The Dph_SCS sample exhibited finer particles with better uniformity and dispersity than that of Dph_SCS. These findings were in agreement with previous comparative studies which show that SCS consistently produces finer particles than traditional solid-state methods.[1, 6–8] Surface area measurements of both samples should be taken in the future to provide a quantitative basis for the observed particle size differences.

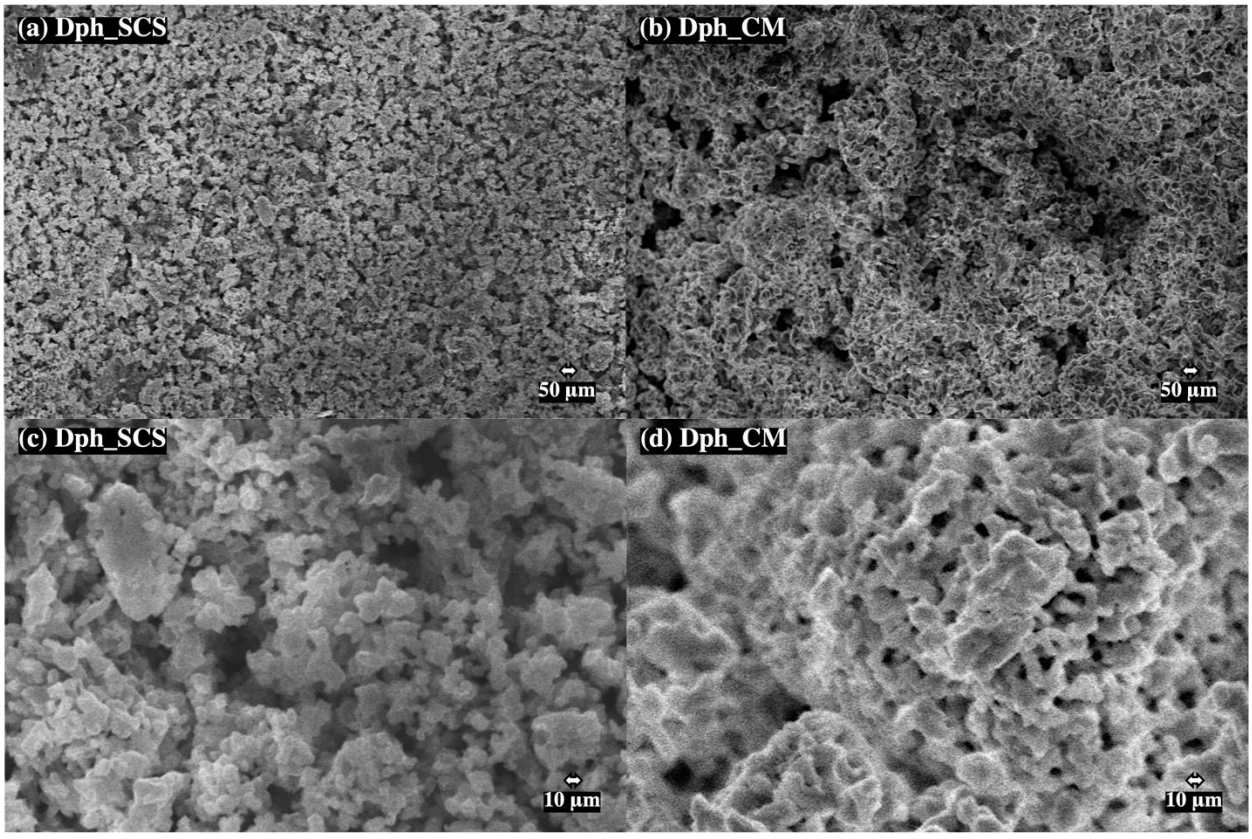

Figure 3-3: Low magnification SEM images of (a) Dph_SCS and (b) Dph_CM; high magnification SEM images of (c) Dph_SCS and (d) Dph_CM.

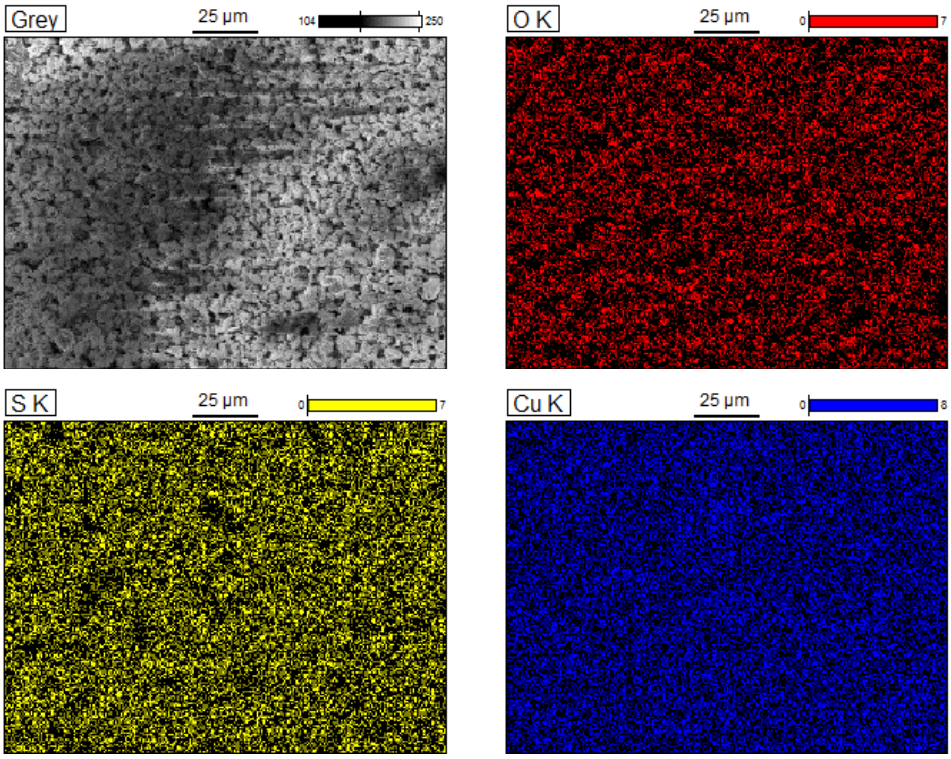

Figure 3-4: EDX elemental maps of Dph_SCS.

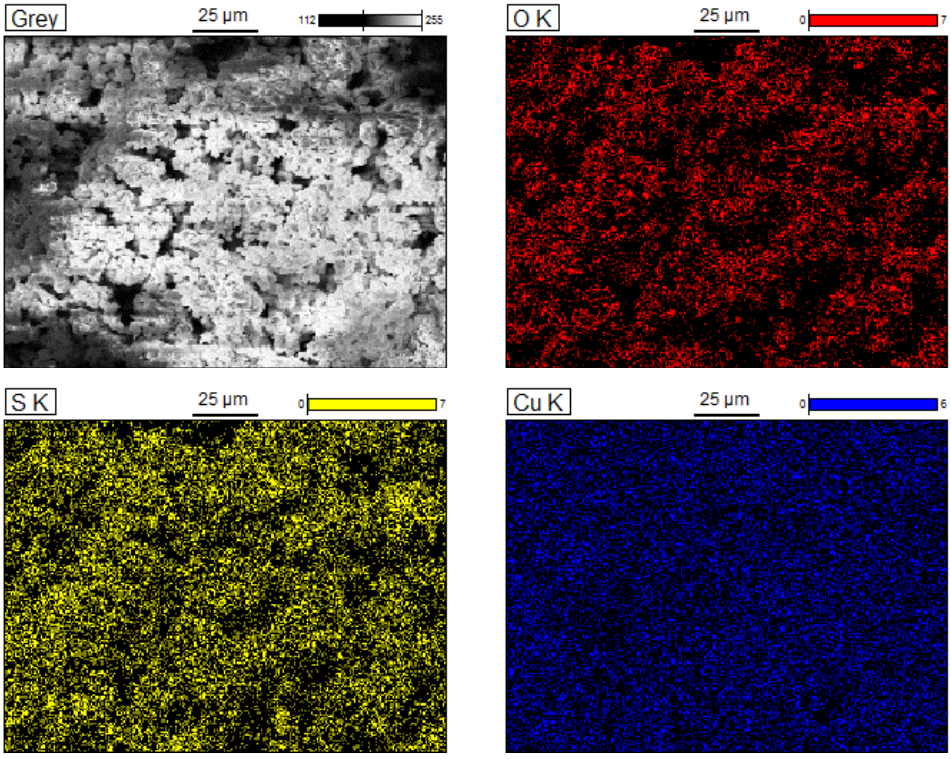

Figure 3-5: EDX elemental maps of Dph_CM.

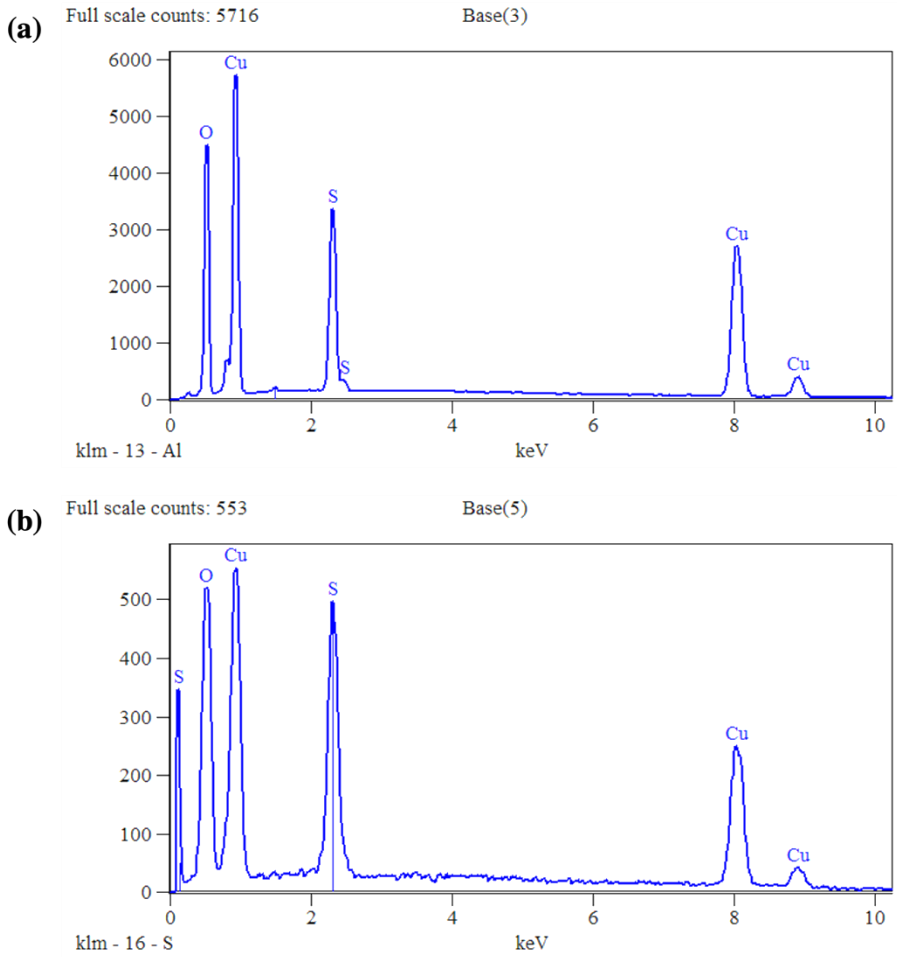

Figure 3-6: EDX spectra of (a) Dph_SCS and (b) Dph_CM.

Despite the differences in the particle size and dispersion, energy-dispersive X-ray spectroscopy (EDX) indicated that copper, oxygen, and sulfur were distributed evenly amongst the surface of both samples without any areas of noticeable elemental vacancy visible. This is evident in the elemental maps of both Dph_SCS (Figure 3-4) and Dph_CM (Figure 3-5). The EDX spectra for both samples are shown in Figure 3-6 and the quantitative results from the analysis are tabulated in Table 3-3. Both samples gave atom concentrations in wt % and at % in reasonable agreement with what is predicted. Interestingly, both compounds exhibited an excess of copper atoms at the surface of the material at the expense of sulfur and oxygen; further experimentation would be needed to investigate the origin of this anomaly. It might be necessary to treat and coat the samples

to reduce the extent of surface conductivity to improve the resolution possible for SEM-EDX in the future.

Table 3-3: Atom concentrations in wt % and at % for Dph_SCS and Dph_CM from EDX.

Atom Concentration		Predicted	Dph_SCS	Dph_CM
wt %	Cu	53.14	59.09 ± 0.51	66.13 ± 2.47
	O	33.45	28.77 ± 0.20	21.68 ± 0.47
	S	13.41	12.15 ± 0.10	12.19 ± 0.32
at %	Cu	25.00	29.92	37.49
	O	62.50	57.88	48.81
	S	12.50	12.20	13.70

Transmission electron microscopy (TEM) and selective area electron diffraction (SAED) images were taken to provide further confirmation of the synthesis of phase-pure dolerophanite in both samples. Low magnification TEM images are shown in Figure 3-7; once again it was observed that Dph_SCS exhibited finer particles than that of Dph_CM.

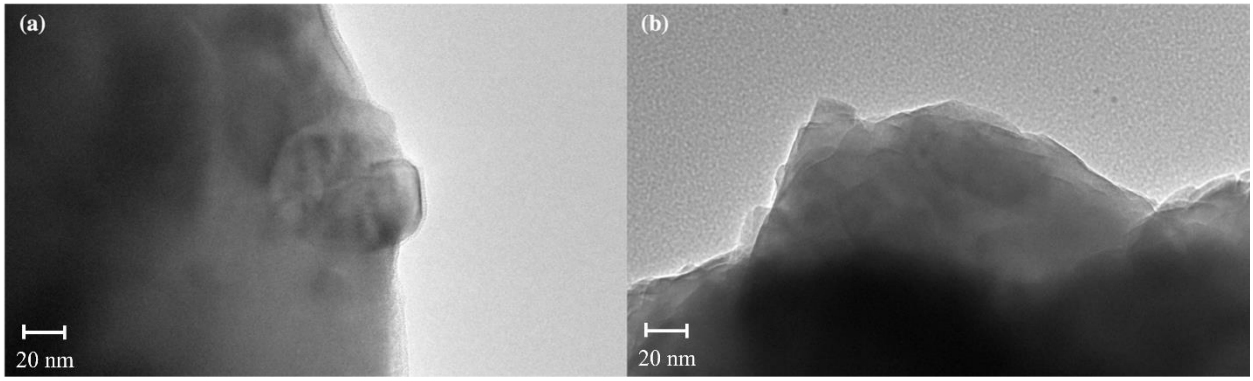

Figure 3-7: Low magnification TEM images of (a) Dph_SCS and (b) Dph_CM.

SAED patterns for both samples are shown in Figure 3-8; the indexed planes in these images, along with the corresponding 2θ values, measured *d*-spacings, and *d*-spacings calculated via refinement are listed in Table 3-4. The TEM–SEM data showed good agreement with literature[9]

and corroborated the phase purity of both samples obtained in this study via SCS and CM synthesis.

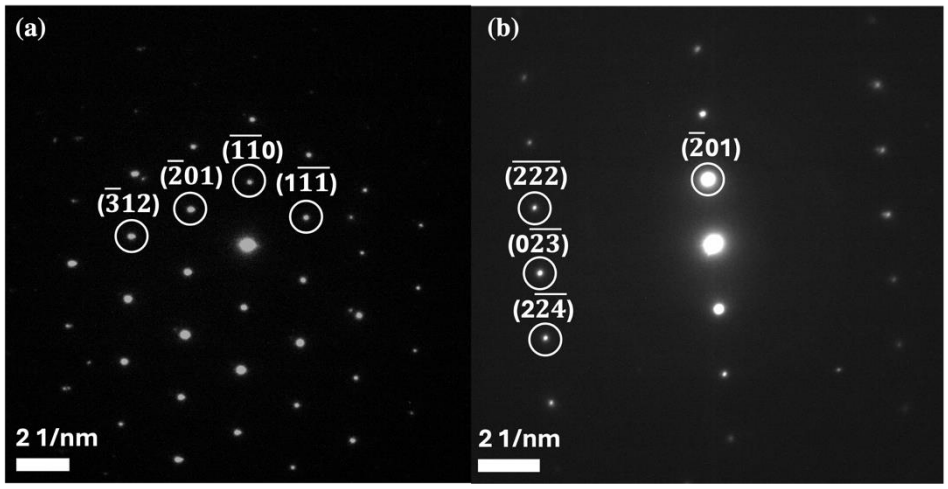

Figure 3-8: SAED patterns for (a) Dph_SCS and (b) Dph_CM.

Table 3-4: *hkl* indexing and *d*-spacing of planes observed in the SAED of Dph_SCS and Dph_CM.

			***d*-spacing (Å)**					***d*-spacing (Å)**	
Sample	**2θ**	***hkl***	**Refinement**	**Measured**	**Sample**	**2θ**	***hkl***	**Refinement**	**Measured**
Dph_ SCS	18.0º	$\bar{1}\bar{1}0$	4.943	4.850	Dph_ CM	19.0º	$\bar{2}01$	4.668	4.592
	18.7º	$1\bar{1}\bar{1}$	4.769	4.689		51.2º	$0\bar{2}\bar{3}$	1.780	1.686
	19.0º	$\bar{2}01$	4.668	4.594		53.6º	$\bar{2}\bar{2}\bar{2}$	1.707	1.626
	33.5º	$\bar{3}12$	2.685	2.632		56.6º	$2\bar{2}\bar{4}$	1.623	1.544

3.2 Thermal Analysis

Thermogravimetric analysis (TGA) was first used to help explore the post-SCS annealing profile (cf., Figure 2-2) with pXRD to confirm observed phases. The spectra for the powder that resulted directly from the SCS process qualitatively demonstrated a low-crystallinity sample consisting of an anhydrous copper (II) sulfate major phase and a dolerophanite minor phase. This indicated that the self-propagating combustion was sufficiently exothermic to produce dolerophanite at a relatively low temperature.[1]

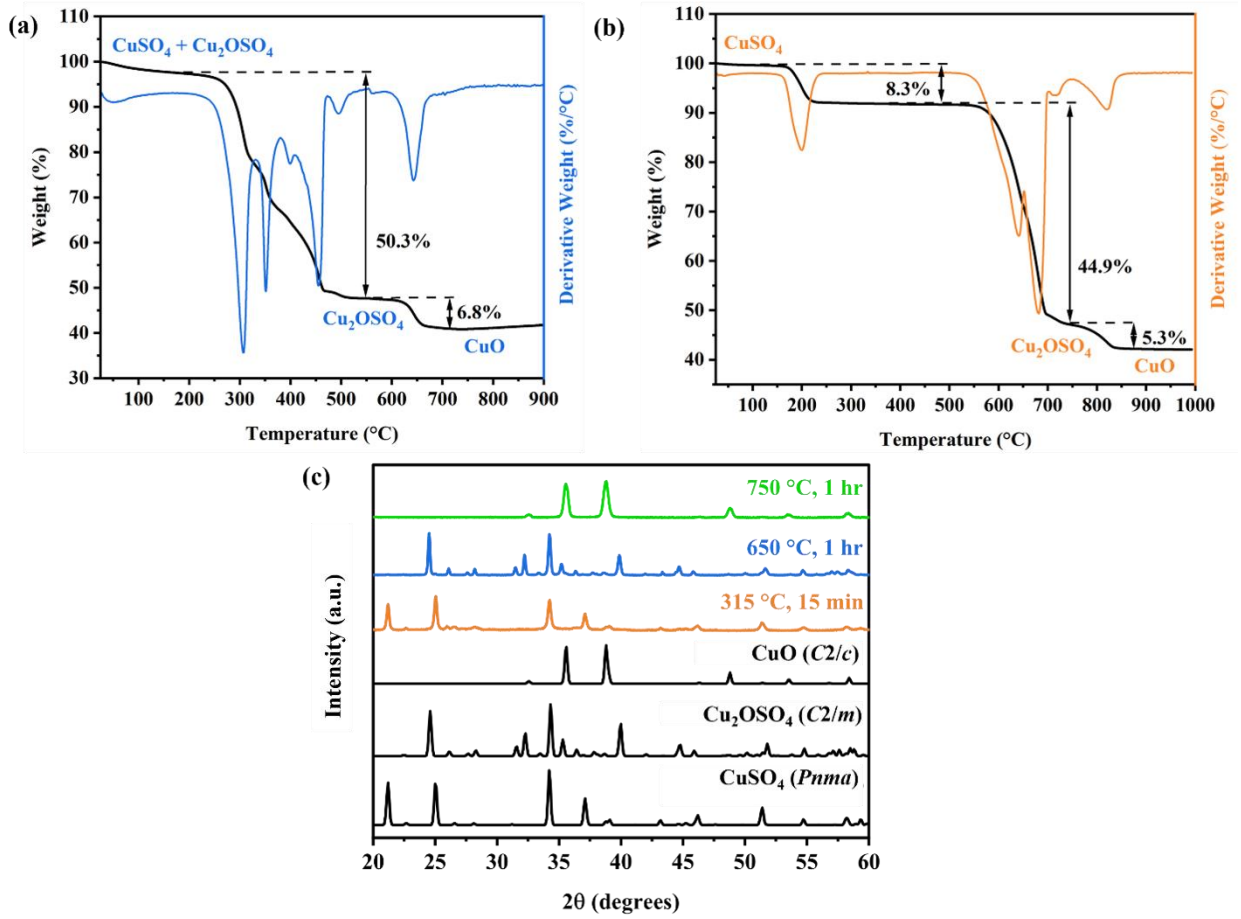

Figure 3-9: (a) TGA profile of the SCS product; (b) TGA profile of a reference anhydrous copper (II) sulfate sample; (c) pXRD spectra of the annealed products. Reference spectra taken from ref 3, 4, and 10.

TGA was performed on this "crude" SCS product and a reference anhydrous copper (II) sulfate sample from room temperature to 1000 ºC at a heating rate of 2 ºC/min under nitrogen. Comparing the resulting thermograms (Figures 3-9a and 3-9b), both samples exhibited a thermal decomposition pathway from $CuSO_4$ to Cu_2OSO_4 to CuO; however, the onset temperatures for these processes differed quite noticeably between the two samples. The reference sample began the decomposition to dolerophanite at ~600 ºC and then to copper (II) oxide at ~800 ºC; these same decompositions for the SCS samples had consistently lower onset temperatures of ~300 ºC and ~625 ºC, respectively. It should be noted that other studies have found that SCS products can undergo thermal processes such as sintering at temperatures lower than what is needed to achieve

the same process on compounds produced by traditional solid-state synthesis.[11] Further studies are required to suggest mechanisms for the decompositions observed in Figures 3-9a and 3-9b.

TGA and differential scanning calorimetry (DSC) were performed on the thermally treated Dph_SCS sample from room temperature to 1000 ºC at a heating rates ranging 5–20 ºC/min. The TGA thermogram (Figure 3-10a) showed that the dolerophanite remained thermally stable until ~670 ºC at which point it began to decompose to copper (II) oxide and then at ~825 ºC it began to decompose to copper (I) oxide. These two events were labeled as T_{p1} and T_{p2}, respectively. These new data contrast with previous findings[5] that dolerophanite began thermal decomposition at 925 ºC; within the context of this previous work, the reported decomposition was likely the secondary decomposition to *copper (I) oxide*.

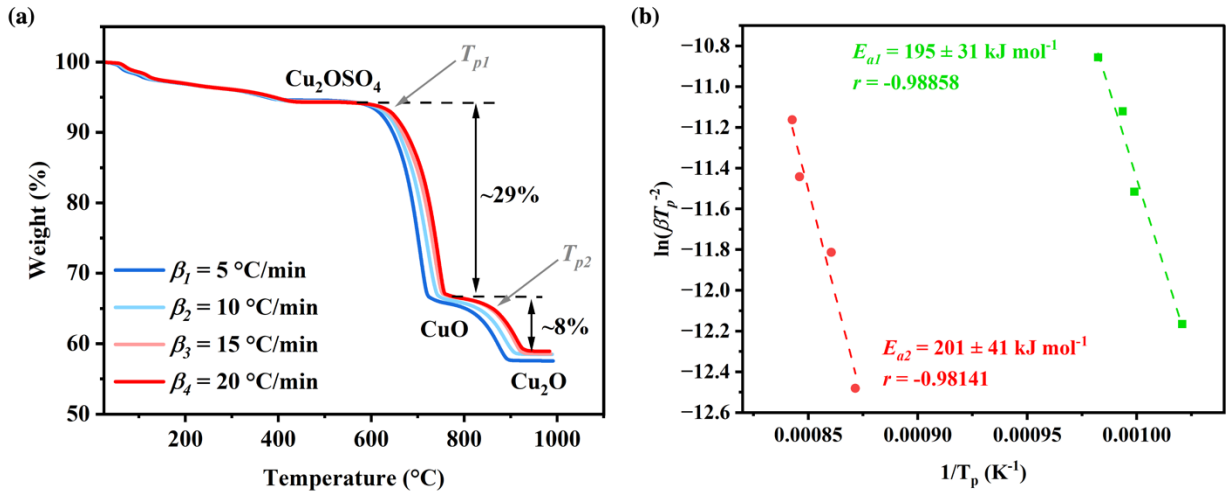

Figure 3-10: (a) TGA of phase-pure dolerophanite with varying heating rates, β; (b) activation energies estimated by the Kissinger equation.

Using the Kissinger equation (cf., Equation 2.1), estimates for the activation energies for the decomposition of dolerophanite to copper (II) oxide and to copper (I) oxide were E_a = 195 ± 31 kJ mol^{-1} and E_a = 201 ± 41 kJ mol^{-1} (Figure 3-10b). It is suggested that this first activation energy represents the energy barrier for the release of sulfur trioxide gas due to the breaking of

bonds between the $(SO_4)^{2-}$ tetrahedra and the [OCu(II)$_4$] "backbone" (cf., Figure 1-4) upon sufficient anisotropic thermal expansion. The observed mass loss for this transition (~29 wt %) closely aligned with the predicted mass loss (~33 wt %) for this proposed fist-order decomposition mechanism (Equation 3.3).

$$Cu_2OSO_4(s) \xrightarrow{\Delta} 2CuO(s) + SO_3(g) \tag{3.3}$$

It is also suggested that this second activation energy represents the energy barrier for the release of oxygen gas due the breaking of the Cu–O bonds in the "backbone" upon sufficient anisotropic thermal expansion. The observed mass loss for this transition (~7 wt %) closely aligned with the predicted mass loss (~8 wt %) for this proposed first-order decomposition mechanism (Equation 3.4).

$$2CuO(s) \xrightarrow{\Delta} Cu_2O(s) + \frac{1}{2}O_2(g) \tag{3.4}$$

A summary of both of the observed decomposition processes is provided in Table 3-5.

Table 3-5: Mass loss and activation energy for two proposed thermal decompositions of dolerophanite.

Decomposition Reaction	**Mass Loss (w.r.t. Dolerophanite)**		E_a
	Predicted (wt %)	**Observed (wt %)**	**(kJ mol^{-1})**
$Cu_2OSO_4(s) \rightarrow 2CuO(s) + SO_3(g)$	33	29	195 ± 31
$2CuO(s) \rightarrow Cu_2O(s) + ½O_2(g)$	7	8	201 ± 41

3.3 Spectroscopic Analysis

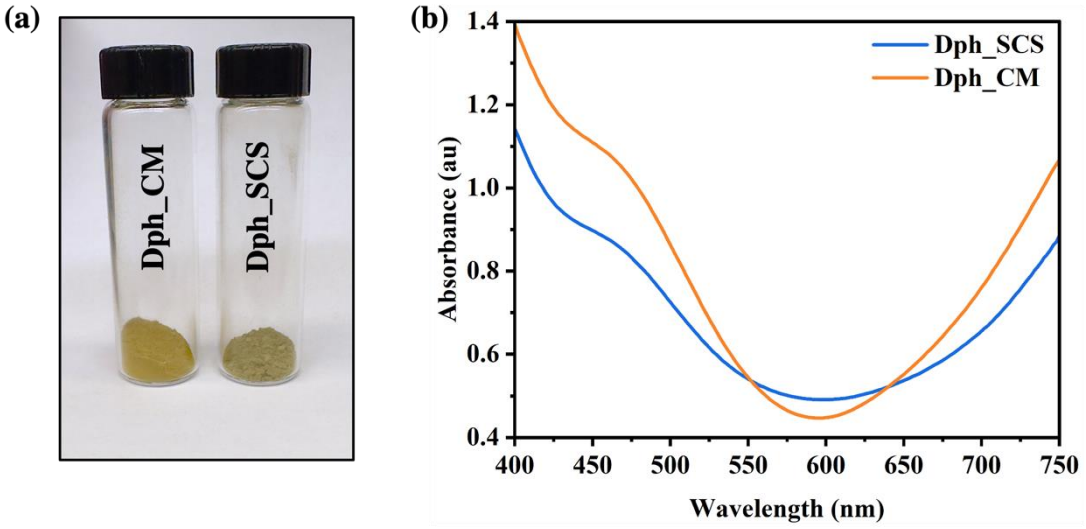

Figure 3-11: (a) Physical appearance of Dph_SCS and Dph_CM; (b) UV-vis spectra of both samples

Visually, there was a distinct difference in color between the CM-derived and the SCS-derived dolerophanite samples; Dph_CM appeared as a bright yellow powder whereas Dph_SCS appeared more as a yellow-grey powder (Figure 3-11a). When considering the UV-vis absorbance spectra of the two samples (Figure 3-11b), this difference manifests with Dph_CM giving a sharper peak with a greater absorbance than Dph_SCS. The analytical wavelength of Dph_CM, λ_{max} = 594 nm, was slightly shorter than that of Dph_SCS, λ_{max} = 600 nm.

Utilizing the Kubelka-Munk transformation (cf. Equation 2.2 and 2.3) of the diffuse reflectance data of both samples, Tauc plots were generated to consider both direct and indirect bandgap optical transitions (Figure 3-12a and 3-12b, respectively). In both Tauc plots, Dph_SCS and Dph_CM exhibited sharp linear increases in the reflectance response characteristic of semiconducting materials. Extrapolating this linear response to the baseline provides an estimation of the optical bandgap energies.[12]

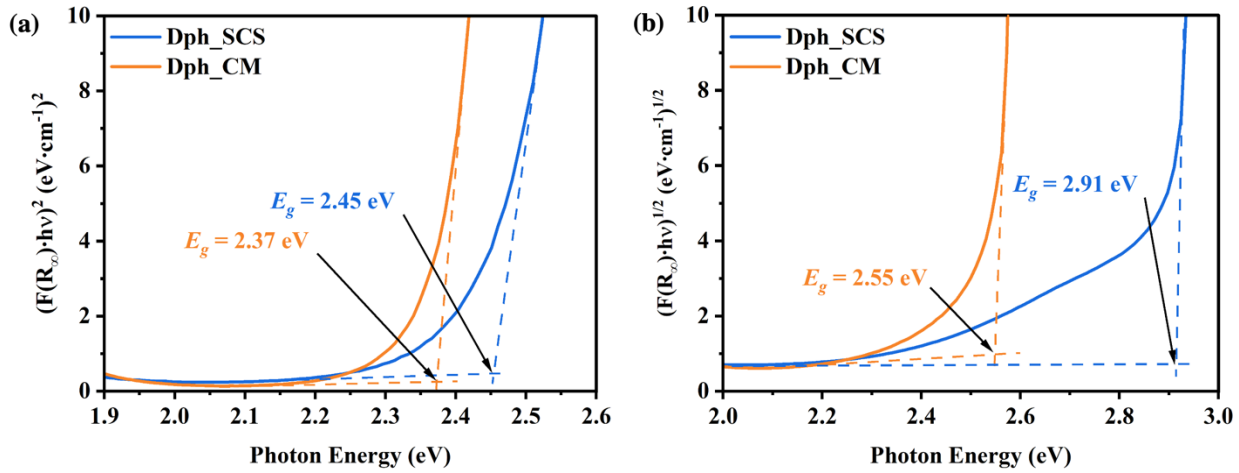

Figure 3-12: (a) Direct and (b) indirect bandgap optical transitions estimated using the Kubelka-Munk transformation of the Tauc equation.

From the Tauc plots, there was a clear shift of the optical bandgap energies as a result of the chosen synthesis pathways. CM synthesis yielded samples with lower optical bandgap energies, E_g, with a direct transition of E_g = 2.37 eV and an indirect transition of E_g = 2.55 eV while SCS yielded samples with direct and indirect transitions of E_g = 2.45 eV and E_g = 2.91 eV, respectively. These trends suggest a route to optical bandgap engineering based on the strategy chosen to synthesize dolerophanite. Considering the physical characterization of the two samples, the differences in the observed optical bandgaps may originate from a particle size effect as Dph_SCS had the higher energy optical transitions and the apparent smaller average particle size.

Fourier transform infrared spectroscopy (FTIR) was performed on the SCS dolerophanite sample and of a reference anhydrous copper (II) sulfate sample (Figure 3-13a). Particular comparison of the broad intense peak centered at around 1058 cm^{-1}, assigned to S–O bonding,[13] was used as a fingerprint to distinguish between the two copper (II) sulfate minerals. Comparison of peaks at 438 cm^{-1} and 590 cm^{-1}, assigned to Cu–O bonding (ref 14), helped further distinguish between the two minerals.

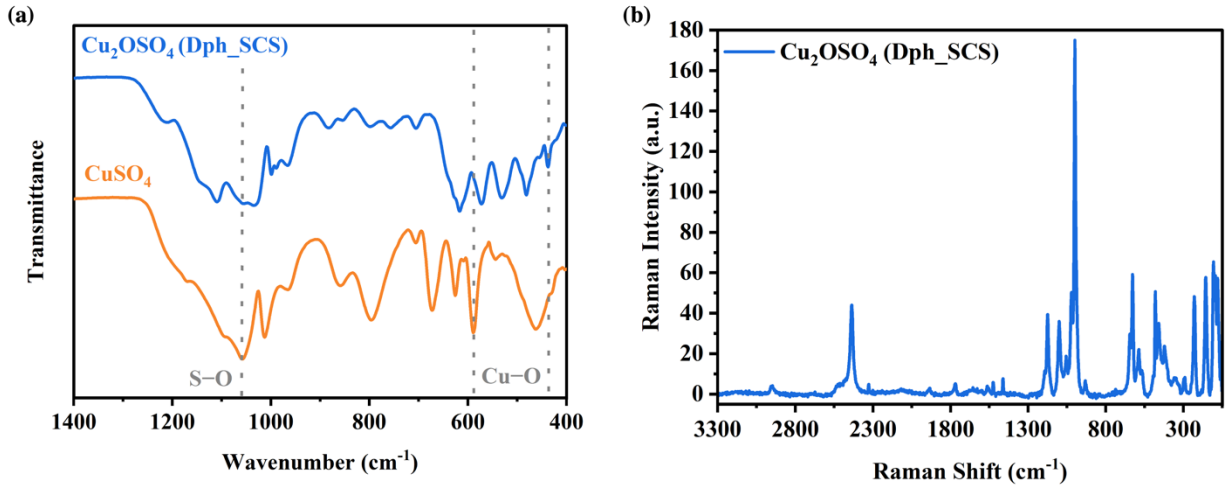

Figure 3-13: (a) FTIR spectra of dolerophanite and reference anhydrous copper (II) sulfate; (b) Raman spectra of dolerophanite taken with a 532 nm laser.

Raman spectra were taken for dolerophanite (Figure 3-13b), and the suggested assignments were determined by comparison to known Raman bands for anhydrous copper (II) sulfate taken from ref 15. Table 3-6 lists the observed bands for dolerophanite, the reference bands for anhydrous copper (II) sulfate, and the suggested assignments.

In the region between 900 and 1060 cm^{-1} (Figure 3-14a), sharp bands were observed at 999.5 and 1022 cm^{-1} as well as less intense bands at 933 and 1056.5 cm^{-1} which correlated closely with previously reported bands at 932 and 1057 cm^{-1} corresponding to $\nu_1[SO_4^{2-}]$ symmetric stretching modes.[15] In the region between 1060 and 1400 cm^{-1} (Figure 3-14b) there was an intense band at 1101 cm^{-1} and two convoluted intense bands at 1175 and 1193.5 cm^{-1} which both correlated with previously reported bands at 1174 and 1197 cm^{-1} corresponding to $\nu_3[SO_4^{2-}]$ antisymmetric stretching modes; absent was a band correlating with the known ν_3 at 1162.5 cm^{-1}.[15]

In the region between 50 and 550 cm^{-1} (Figure 3-14c) there were a variety of bands, many of which were overlapping; only the observed bands at 459.5 and 495 cm^{-1} correlated with previously reported bands at 458.5 and 497 cm^{-1} corresponding to $\nu_2[SO_4^{2-}]$ symmetric bending

modes.[15] Other observed bands in this region may be attributed to factors such as local stress and crystal orientation effects which have been observed in the Raman spectra of other copper sulfate minerals.[16]

Table 3-6: Observed Raman shifts (reported in units of cm^{-1}) and suggested band assignments for dolerophanite.

Cu_2OSO_4	$CuSO_4$ (ref 15)	Suggested Assignment
59.5	—	*n.a.*
81	—	
95	—	
108	—	
158	—	
230	—	
291	—	
422	—	$v_2[SO_4^{2-}]$
459.5	458.5	
481	—	
495	497	
568.5	—	$v_4[SO_4^{2-}]$
588	583	
602	605	
627.5	—	
645	—	
933	932	$v_1[SO_4^{2-}]$
999.5	—	
1022	—	
1056.5	1057	
1101	—	$v_3[SO_4^{2-}]$
—	1162.5	
1175	1174	
1193.5	1197	

n.a. = not assigned

Lastly, in the region between 550 and 850 cm^{-1} (Figure 3-14d) there were two sets of convoluted bands, including ones at 588 and 602 cm^{-1} which correlated closely with bands at 583 and 605 cm^{-1} corresponding to $v_4[SO_4^{2-}]$ antisymmetric bending modes.[15] The observed bands beyond 1400 cm^{-1} that are not tabulated in Table 3-6 are difficult to assign due to lack of

corresponding bands in the known spectra for anhydrous copper (II) sulfate and other copper sulfate minerals. Some of the observed bands may arise from sulfate stretching overtones, but further assignments would require more sensitive instrumentation, computational studies, or a combination of both.

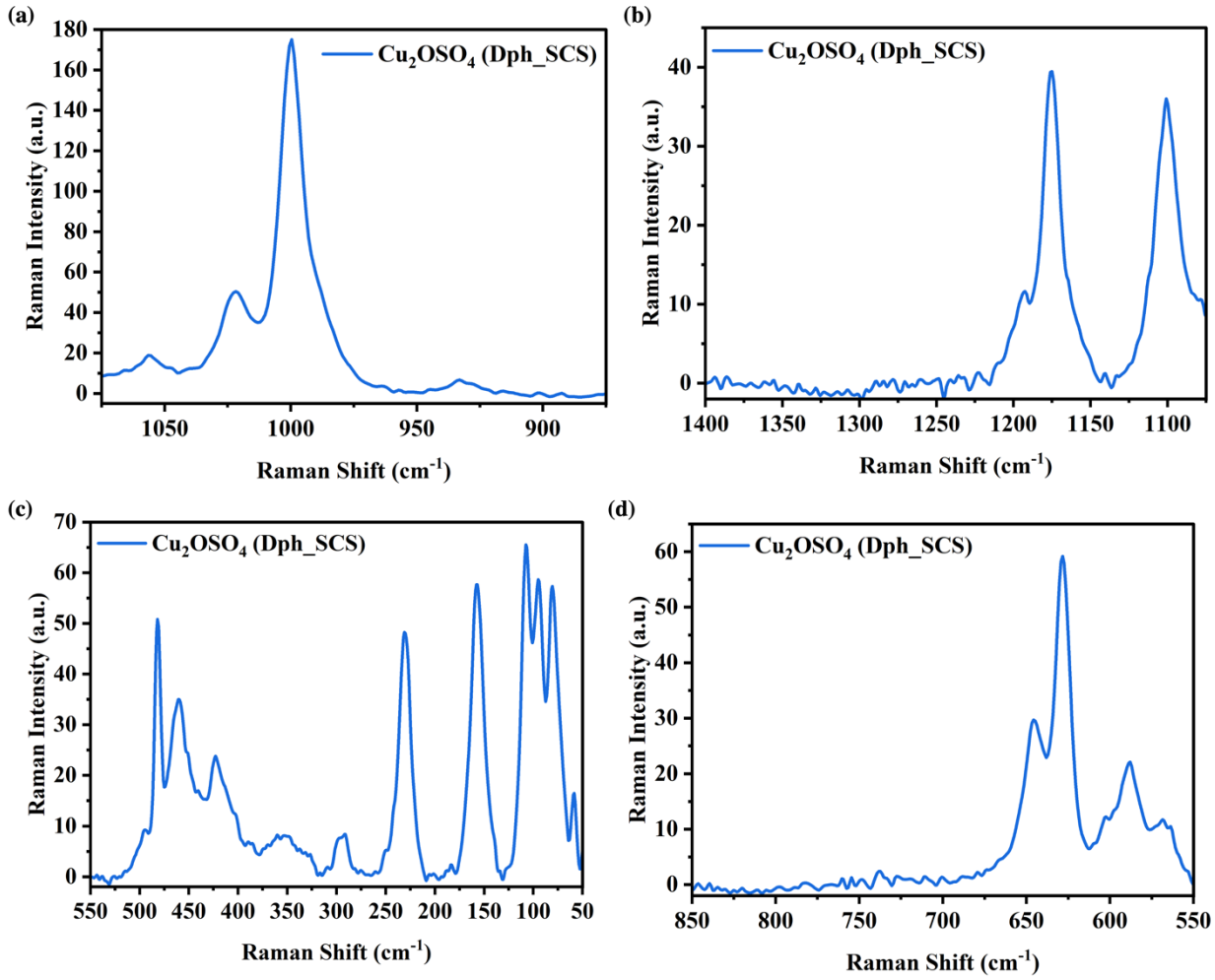

Figure 3-14: Raman spectra of dolerophanite focusing on regions associated with (a) ν_1 symmetric stretching, (b) ν_3 antisymmetric stretching, (c) ν_2 symmetric bending, and (d) ν_4 antisymmetric bending modes of the $(SO_4)^{2-}$ tetrahedra.

3.4 Electronic Band Structure Calculations

Preliminary collinear magnetic calculations were performed, confirming an antiferromagnetic couple ground state with ferrimagnetically-coupled copper atoms within the Kagome-like lattice, agreeing with previously reported magnetic studies of dolerophanite (cf., Figure 1-5). Also in agreement with previous findings, non-magnetic and magnetic density functional theory (DFT) calculations without the Hubbard U or exchange coupling J parameters indicated that dolerophanite was metallic (cf., Figure 1-3). A more in-depth look into the magnetic properties of dolerophanite are, however, outside the scope of this work; ref 17 provides both a good overview of the most current understanding of the magnetic properties of dolerophanite as well as computational studies to support the most current findings. This section instead aims to focus on bulk sample lattice parameters and the projected density of state (PDOS) calculations.

Table 3-7: Comparison of reference, experimental, and computational lattice parameter values for dolerophanite.

Sample	a (Å)	b (Å)	c (Å)	α (°)	β (°)	γ (°)	V(Å^3)
DFT	9.3625	6.3084	7.7458	90.00	123.164	90.00	—
DFT+U+J	9.4291	6.3085	7.6947	90.00	122.539	90.00	—
HSE	9.3645	6.3081	7.7488	90.00	123.539	90.00	—
Dph_SCS	9.39268	6.33669	7.66604	90.000	122.407	90.000	385.211
Dph_CM	9.39229	6.33434	7.66131	90.000	122.385	90.000	384.910
Ref 3	9.370	6.319	7.639	90.00	122.34	90.00	382.1
Ref 5	9.3993	6.3391	7.6688	90.00	122.434	90.00	385.65

Table 3-6 presents the computationally derived lattice parameters; compared to the parameters found in literature[17] and experimentally determined in this work, there is close agreement for all of the parameters. In what follows, DFT indicates calculations without further parameters; DFT+U+J additionally considers a Hubbard U parameter of U = 8.5 eV and an exchange couple J parameter of J = 1.0 eV applied to the 3*d* orbitals of copper. Finally, HSE indicates the use of the Heyd–Scuseria–Ernzerhof hybrid functional.

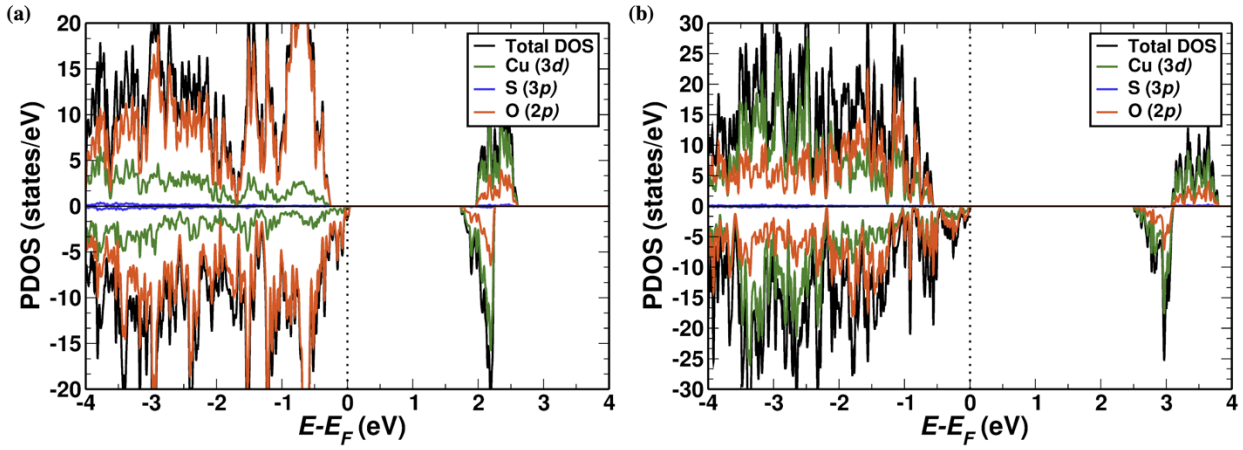

Figure 3-15: PDOS of dolerophanite via (a) DFT+U+J and (B) HSE calculations.

The PDOS computed by both DFT+U+J and HSE gave generally the same band structure for dolerophanite (Figure 3-15a and 3-15b, respectively). The 3*p* band of sulfur contributed little to the PDOS, yielding only slight contributions at around –2 eV relative to the Fermi level and below. This is consistent with the findings of ref 11 (cf., Figure 1-3). The major contributors to the conduction band (CB) edge are shown to be the oxygen 2*p* band and the copper (II) 3*d* band; this, too, is consistent with former studies.[17] Where the current studies differed with previous studies, however, is in the semiconducting nature of dolerophanite. Both our DFT+U+J and HSE calculations indicated the presence of a direct-transition electronic bandgap; DFT+U+J predicted a bandgap of around E_g = 1.75 eV, and HSE predicts a bandgap of around E_g = 2.50 eV. This bandgap was not observed in the previous computation study on this material.[17] The HSE bandgap here agreed closely with the optical bandgap of E_g = 2.45 eV estimated by the Kubelka-Munk transformation of the Tauc equation (cf. Figure 3-7). As was the case with the CB edge, it is demonstrated that the oxygen 2*p* band and the copper (II) 3*d* band are the major contributors to the PDOS at the valence band (VB) edge. No contribution from the sulfur 3*p* was observed at the VB edge.

3.5 References

(1) Varma, A.; Mukasyan, A. S.; Rogachev, A. S.; Manukyan, K. V. Solution Combustion Synthesis of Nanoscale Materials. *Chem. Rev.* **2016**, *116*, 14493–14586.

(2) Binder, O. Definition Des Sulfates Basiques de Cuivre. *Ann. Chim.* **1936**, *5*, 337–409.

(3) Effenberger, H. $Cu_2O(SO_4)$, Dolerophanite: Refinement of the Crystal Structure, with a Comparison of $[OCu(II)_4]$ Tetrahedra in Inorganic Compounds. *Montash. Chem.* **1985**, *116*, 927–931.

(4) Wildner, M.; Giester, G. Crystal Structure Refinements of Synthetic Chalcocyanite ($CuSO_4$) and Zincosite ($ZnSO_4$). *Miner. Petrol.* **1988**, *39*, 201–209.

(5) Nazarchuk, E. V.; Siidra, O. I.; Filatov, S. K.; Charkin, D. O.; Zhdanova, L. R. Thermal Expansion of Anhydrous Copper Sulfate Minerals Determined by Single Crystal X-Ray Diffraction: Chalcocyanite $CuSO_4$, Dolerophanite Cu_2OSO_4 and Kamchatkite $KCu_3O(SO_4)_2Cl$. *Phys. Chem. Miner.* **2023**, *50*, 11–19.

(6) Kim, G.; Lee, N.; Kim, K. B.; Kim, B. K. Chang, H.; Song, S. J.; Park, Y. J. Various Synthesis Methods of Aliovalent-Doped Ceria and Their Electrical Properties for Intermediate Temperature Solid Oxide Electrolytes. *Int. J. Hydrogen Energy* **2023**, *38*, 1571–1587.

(7) Kormányos, A.; Thomas, A.; Huda, M. N.; Sarker, P.; Ping Liu, J.; Poudyal, N.; Janáky, C.; Rajeshwar, K. Solution Combustion Synthesis, Characterization, and Photoelectrochemistry of $CuNb_2O_6$ and $ZnNb_2O_6$ Nanoparticles. *J. Phys. Chem. C* **2016**, *120*, 16024–16034.

(8) Thomas, A.; Janáky, C.; Samu, G. F.; Huda, M. H.; Sarker, P.; Ping Liu, J.; van Nguyen, V.; Wang, E. H.; Schug, K. A.; Rajeshwar, K. Time- and Energy-Efficient Solution Combustion Synthesis of Binary Metal Tungstate Nanoparticles with Enhanced Photocatalytic Activity. *ChemSusChem* **2015**, *8*, 1652–1663.

(9) Mrose, M. E. Vernadskite Discredited: Pseudomorphs of Antlerite After Dolerophanite. *Am. Min.* **1961**, *46*, 146–154.

(10) Åsbrink, S.; Norby, L.-J. A Refinement of the Crystal Structure of Copper (II) Oxide with a Discussion on Some Exceptional E.s.d.'s. *Acta. Cryst.* **1970**, *26*, 8–15.

(11) Matovic, B.; Bucevac, D.; Jiraborvornpongsa, N.; Yoshida, K.; Yano, T. Synthesis and Characterization of Nanometric Strontium-Doped Ceria Solid Solutions via Glycine-Nitrate Procedure. *J. Ceram. Soc. Jpn.* **2012**, *120*, 69–73.

(12) Makula, P.; Pacia, M.; Macyk, W. How to Correctly Determine the Band Gap Energy of Modified Semiconductor Photocatalysts Based on UV-Vis Spectra. *J. Phys. Chem. Lett.* **2018**, *9*, 6814–6817.

(13) Guo, X.; Xu, Y.; Zha, F.; Tang, X.; Tian, H. α-Fe_2O_3/$Cu_2O(SO_4)$ Composite as a Novel and Efficient Heterogeneous Catalyst for Photo-Fenton Removal of Orange II. *Appl. Surf. Sci.* **2020**, *530*, 147144.

(14) Elango, M.; Deepa, M.; Subramanian, R.; Musthafa, A. M. Synthesis, Characterization, and Antibacterial Activity of Polyindole/Ag-CuO Nanocomposites by Reflux Condensation Method. *Polym.-Plast. Technol.* **2017**, *57*, 1440–1451.

(15) Fu, X.; Yang, G.; Sun, J.; Zhou, J. Vibrational Spectra of Copper Sulfate Hydrates Investigated with Low-Temperature Raman Spectroscopy and Terahertz Time Domain Spectroscopy. *J. Phys. Chem. A* **2012**, *116*, 7314–7318.

(16) Martens, W.; Frost, R. L.; Kloprogge, J. T.; Williams, P. A. Raman Spectroscopic Study of the Basic Copper Sulphates – Implications for Copper Corrosion and 'Bronze Disease'. *J. Raman Spectrosc.* **2003**, *24*, 145–151.

(17) Panther, A.; Tsirlin, A.; Rousochatzakis, I. Frustration Relief and Reorientation Transition in the Kagome-Like Dolerophanite Cu_2OSO_4. *Phys. Rev. B* **2023**, *108*, 224410.

CHAPTER 4: CONCLUSIONS AND FUTURE WORK

4.1 Conclusions

Fumarolic mineral dolerophanite Cu_2OSO_4 was synthesized as a minor phase along with anhydrous copper (II) sulfate via the solution combustion synthesis (SCS) of copper (II) nitrate hemi(pentahydrate) and thiourea at 315 ºC using an oxidant-to-fuel ratio of 1:1; post-SCS annealing at 650 ºC yielded phase-pure dolerophanite as a yellow-grey powder. Typical yield from this synthesis was ~80%. To provide a way to compare SCS to traditional solid-state synthesis, a second sample of dolerophanite was synthesized via ceramic method (CM) synthesis by heating anhydrous copper (II) sulfate at 650 ºC, yielding phase-pure dolerophanite as a bright-yellow powder.

Powder X-ray diffraction (pXRD) confirmed the monoclinic *C*2/*m* crystal structure of dolerophanite, and Rietveld refinement of the diffraction powder indicated that the experimentally observed lattice parameters were in excellent agreement with previously reported values.[1, 2] Scanning electron microscopy- energy-dispersive X-ray spectroscopy (SEM–EDX) showed that dolerophanite produced by SCS exhibited finer and more dispersed particles than that produced by CM synthesis; both samples exhibited homogeneous elemental dispersion. Transmission electron microscopy-selective area electron diffraction (TEM–SAED) was used to further corroborate phase purity and provided *hkl* indices and *d*-spacings which were in good agreement with literature.[3]

Thermogravimetric analysis (TGA) and differential scanning calorimetry (DSC) indicated that dolerophanite underwent thermal decomposition to copper (II) oxide at ~670 ºC and then to

copper (I) oxide at ~825 ºC. The Kissinger first-order kinetics model[4, 5] afforded estimates of the activation energies of E_a = 195 ± 31 kJ mol^{-1} and E_a = 201 ± 41 kJ mol^{-1}, respectively, for these decompositions and mechanistic pathways were proposed for both decompositions.

Dolerophanite was shown to exhibit strong absorbance in the ultraviolet-visible (UV-vis) range with an analytical wavelength ~600 nm. Kubelka-Munk transformed Tauc analysis[6, 7] indicated that the material possessed both direct and indirect optical bandgap transitions and that different synthesis strategies yielded noticeable differences in these optical bandgaps. Dolerophanite from ceramic method (CM) synthesis yielded a direct optical transition of E_g = 2.37 eV and an indirect optical transition of E_g = 2.55 eV; dolerophanite from SCS yielded direct and indirect optical transitions of E_g = 2.45 eV and E_g = 2.91 eV, respectively. Differences in these observed optical transitions were attributed to a particle size effect. Projected density of states (PDOS) calculations using the Heyd–Scuseria–Ernzerhof hybrid functional (HSE)[8] agreed with these experimental data, predicting an electronic bandgap of E_g = 2.50 eV with the oxygen 2*p* band and the copper 3*d* band serving as the major contributors to both the conduction band (CB) and valence band (VB) edges.

In the Fourier transformed infrared spectra, dolerophanite exhibited a characteristic broad peak at around 1058 cm^{-1}, attributed to S–O bonding, as well as a peak at around 438 cm^{-1}, attributed to Cu–O bonding. In the Raman spectra, sulfate anion ν_1 (symmetric stretching) modes were observed at 933, 999.5, 1022, and 1056.5 cm^{-1}; ν_2 (symmetric bending) at 422, 459.5, 481, and 495 cm^{-1}; ν_3 (antisymmetric stretching) at 1101, 1175, and 1193.5 cm^{-1}; and ν_4 (antisymmetric bending) at 568.5, 588, 602, 627.5, and 645 cm^{-1}.

4.2 Suggested Future Work

Preliminary data from this work showed that varying the oxidant-to-fuel ratio for SCS yielded copper (II) oxide. Direct SCS of phase-pure dolerophanite without post-process annealing has yet to be observed. Further modifications of the SCS strategy, such as utilizing sulfurized ethylene glycol as a dispersant in a manner similar to ref 7 and 8, should be explored. Ref 7 and 9 also showed that dolerophanite can be used in the synthesis of composite materials, indicating another synthesis-oriented route of exploration. It may also be possible to use SCS to synthesize other fumarolic copper sulfates such as kamchatkite $KCu_3O(SO_4)_2Cl$ which has been explored briefly.[2]

Suggested further physical characterization of the material includes higher-resolution pXRD to provide improvement of the refinement of the diffraction pattern. Temperature-programmed pXRD using a hot-stage should afford useful insights into thermal evolution of the various phases. Treatment of the samples to reduce surface conduction may prevent astigmatism in high-resolution SEM. Options for further spectroscopic or analytical characterization include the use of X-ray photoelectron spectroscopy (XPS) or inductively coupled plasma-optical emission spectroscopy (ICP-OES) for more detailed quantitative analysis of elemental concentrations. Additional density functional theory (DFT) studies may be useful in further understanding and simulation of the observed Raman spectra as well as providing phonon and normal coordinate analysis.

Other preliminary data from this work showed that dolerophanite yielded no photoelectrochemical (PEC) activity, nor did it fluoresce. Dolerophanite has, however, been shown to exhibit photocatalytic activity via photo-Fenton degradation of Orange II dye.[7] This is a promising avenue for exploration and well-established experiments such as the bleaching of

lignin[10] could be employed. Ref 9 also indicated that exploration of dolerophanite as an electrode material Li-ion batteries is an intriguing avenue due to its ability to access the $Cu^{2+/3+}$ redox couple. Either application of the material would contribute meaningfully to the overall literature seeing as only the magnetic properties of dolerophanite have been thoroughly explored.[11]

In summary, dolerophanite is a fascinating material and, considering the limited literature on the material, it offers promising avenues for continued experimentation and exploration.

4.3 References

(1) Effenberger, H. $Cu_2O(SO_4)$, Dolerophanite: Refinement of the Crystal Structure, with a Comparison of $[OCu(II)_4]$ Tetrahedra in Inorganic Compounds. *Montash. Chem.* **1985**, *116*, 927–931.

(2) Nazarchuk, E. V.; Siidra, O. I.; Filatov, S. K.; Charkin, D. O.; Zhdanova, L. R. Thermal Expansion of Anhydrous Copper Sulfate Minerals Determined by Single Crystal X-Ray Diffraction: Chalcocyanite $CuSO_4$, Dolerophanite Cu_2OSO_4 and Kamchatkite $KCu_3O(SO_4)_2Cl$. *Phys. Chem. Miner.* **2023**, *50*, 11–19.

(3) Mrose, M. E. Vernadskite Discredited: Pseudomorphs of Antlerite After Dolerophanite. *Am. Min.* **1961**, *46*, 146–154.

(4) Kissinger, H. E. Variation of Peak Temperature with Heating Rate in Differential Thermal Analysis. *J. Res. Natl. Bur. Stand.* **1956**, *57*, 217–221.

(5) Kissinger, H. E. Reaction Kinetics in Differential Thermal Analysis. *Anal. Chem.* **1957**, *29*, 1702–1706.

(6) Kubelka, P.; Munk, F. An Article on Optics of Pain Layers. *Z. Techn. Phys.* **1931**, *12*, 593–599.

(7) Tauc, J.; Grigorovici, R.; Vancu, A. Optical Properties and Electronic Structure of Amorphous Germanium. *Phys. Status Solidi B* **1966**, *15*, 627–537.

(8) Heyd, J.; Scuseria, G. E.; Ernzerhof, M. Hybrid Functionals Based on a Screened Coulomb Potential. *J. Chem. Phys.* **2003**, *118*, 8207–8215.

(9) Guo, X.; Xu, Y.; Zha, F.; Tang, X.; Tian, H. α-Fe_2O_3/$Cu_2O(SO_4)$ Composite as a Novel and Efficient Heterogeneous Catalyst for Photo-Fenton Removal of Orange II. *Appl. Surf. Sci.* **2020**, *530*, 147144.

(10) Sun, R.; Shen, H.; Lv, X.; Wang, Y.; Hu, T. Solution Combustion Synthesis of MgO-Stabilized CaO Sorbents Using Polyethylene Glycol as Fuel and Dispersant. *RSC Adv.* **2024**, *14*, 1741–1749.

(11) Sun, M.; Rousse, G.; Abakumov, A. M.; Saubanère, M.; Doublet, M.-L.; Jose Rodriguez-Carvajal, J.; Tendeloo, G. Van; Tarascon, J.-M.; Rousse, G.; Dou-Blet, M.-L.; Rodríguez-Carvajal, J.; Van Tendeloo, G. $Li_2Cu_2O(SO_4)_2$: A Possible Electrode for Sustainable Li-Based Batteries Showing a 4.7 V Redox Activity vs. Li^+/Li^o. *Chem. Mater*. **2015**, *27*, 3077–3087.

(12) Ohnishi, H.; Masumura, M.; Tsubomura, H.; Iwasaki, M. Bleaching of Lignin Solution by a Photocatalyzed Reaction on Semiconductor Photocatalysts. *Ind. Eng. Chem. Res.* **1989**, *28*, 719–724.

(13) Panther, A.; Tsirlin, A.; Rousochatzakis, I. Frustration Relief and Reorientation Transition in the Kagome-Like Dolerophanite Cu_2OSO_4. *Phys. Rev. B* **2023**, *108*, 224410.